

X-ray Temperature and Mass Measurements to the Virial Radius of Abell 1413 with Suzaku

A. Hoshino,¹ J. P. Henry,² K. Sato,³ H. Akamatsu,¹ W. Yokota,¹ S. Sasaki,¹ Y. Ishisaki,¹ T. Ohashi,¹
M. Bautz,⁴ Y. Fukazawa,⁵ N. Kawano,⁵ A. Furuzawa,⁶ K. Hayashida,⁷ T. Tawa,⁷ J. Hughes,⁸
M. Kokubun,⁹ and T. Tamura⁹

¹ *Department of Physics, Tokyo Metropolitan University,
1-1 Minami-Osawa, Hachioji, Tokyo 192-0397
h_akio@phys.metro-u.ac.jp*

² *Institute for Astronomy, University of Hawaii,
2680 Woodlawn Drive, Honolulu, HI 96822, USA*

³ *Graduate School of Natural Science and Technology,
Kanazawa University, Kakuma, Kanazawa, Ishikawa 920-1192*

⁴ *Kavli Institute for Astrophysics and Space Research, Massachusetts Institute of Technology,
77 Massachusetts Avenue, Cambridge, MA 02139, USA*

⁵ *Department of Physical Science, Hiroshima University,
1-3-1 Kagamiyama, Higashi-Hiroshima, Hiroshima 739-8526*

⁶ *EcoTopia Science Institute and Department of Astrophysics, Nagoya University,
Furo-cho, Chikusa-ku, Nagoya 464-8603*

⁷ *Department of Earth and Space Science, Osaka University,
Toyonaka, Osaka 560-0043*

⁸ *Department of Physics and Astronomy, Rutgers University
136 Frelinghuysen Road, Piscataway, NJ 08854-8019, USA*

⁹ *Department of High Energy Astrophysics, Institute of Space and Astronautical Science,
Japan Aerospace Exploration Agency,
3-1-1 Yoshinodai, Sagamihara, Kanagawa 229-8510*

(Received <reception date>; accepted <acceptation date>)

Abstract

We present X-ray observations of the northern outskirts of the relaxed galaxy cluster A1413 with Suzaku, whose XIS instrument has the low intrinsic background needed to make measurements of these low surface brightness regions. We excise 15 point sources superimposed on the image above a flux of 1×10^{-14} erg cm⁻² s⁻¹ (2–10 keV) using XMM-Newton and Suzaku images of the cluster. We quantify all known systematic errors as part of our analysis, and show our statistical errors encompasses them for the most part. Our results extend previous measurements with Chandra

and XMM-Newton, and show a significant temperature drop to about 3 keV at the virial radius, r_{200} . Our entropy profile in the outer region ($> 0.5 r_{200}$) joins smoothly onto that of XMM-Newton, and shows a flatter slope compared with simple models, similar to a few other clusters observed at the virial radius. The integrated mass of the cluster at the virial radius is approximately $7.5 \times 10^{14} M_{\odot}$ and varies by about 30% depending on the particular method used to measure it.

Key words: galaxies: clusters: individual (Abell 1413) — X-rays: galaxies: clusters — X-rays: ICM

1. Introduction

X-ray observations of intracluster medium (ICM) primarily give density and temperature. Density may be deduced relatively straightforwardly from cluster surface brightness because the ICM is optically thin and the emission coefficient over most observed bandpasses is nearly independent of temperature. There is good agreement on the ICM density over the observed radial range among different observers. In contrast, cluster temperatures have not been measured much beyond about half of the virial radius and, until recently, the shape of the temperature radial profile was a matter of heated debate even to that radius. Now independent measurements using four different observatories are consistent with a factor of ~ 2 decline of the projected temperature from the center to half the virial radius, at least for relaxed clusters (Markevitch et al. 1998; De Grandi & Molendi 2002; Vikhlinin et al. 2005; Piffaretti et al. 2005; Pratt et al. 2007).

In addition to the fundamental density and temperature variables, it is possible to derive additional thermodynamic variables from them, such as pressure and entropy. These derived variables are very useful when trying to understand the gravitational and non gravitational processes that were operative during the formation and evolution of the cluster. With the assumption of hydrostatic equilibrium, the cluster's total mass can also be derived from the ICM temperature and the radial derivatives of temperature and density. While this assumption is not valid for many clusters, X-ray observations are one of the few that can be used to measure such masses.

The cold dark matter (CDM) paradigm combined with numerical simulations predict that the structure of clusters should exhibit self-similar scaling. That is their properties should be the same when scaled appropriately by redshift and the virial radius. This expected behavior occurs because clusters form from scale-free density perturbations and their evolution is mainly set by scale-free gravity, and both of these result because cluster masses are mainly CDM. Among the two most studied scaling relations are the radial profiles of temperature and total mass. The mass profile in particular is named the NFW profile after the authors of one of the original papers on this subject (Navarro et al. 1996). Deviations from the expected scaling in

high-quality data indicate the importance of non gravitational processes and/or unaccounted bias in the data. The temperature profile predicted by numerical simulations shows a significant drop with radius to about one third of the peak value at the virial radius (e.g. Loken et al. 2002; Komatsu & Seljak 2002; Borgani et al. 2004; Roncarelli et al. 2006). Observationally, the temperature profiles are the key factor in deriving the cluster mass profile up to the virial radius. The precise mass profile will allow us to judge the validity of the present CDM framework, and gives assurance for our application of cluster properties to cosmological studies.

For all of the above reasons it is important to extend X-ray cluster temperature measurements beyond the current limit of ~ 0.5 of the virial radius, particularly for relaxed clusters. Suzaku observed several such clusters in these regions, and some of the results have been published including PKS0745–191 (George et al. 2008), A1795 (Bautz et al. 2009), and A2204 (Reiprich et al. 2009). All these clusters show a systematic trend of the temperature dropping to about one third of the central value, broadly consistent with theoretical expectations. However the statistical quality of the data for any individual cluster is limited and we need to look at many others to discern general behavior. The main difficulty for the measurement of ICM properties in the virial region is the low cluster surface brightness, which means that in no energy range does the cluster emission exceed the Galactic foreground plus cosmic X-ray background emission. Careful study of systematic errors is therefore mandatory when trying to assess the ICM properties around the virial radius.

We have made Suzaku observations of A1413, a moderately distant cluster at redshift $z = 0.1427$ (Böhringer et al. 2000) whose size is well suited to our field of view. Assuming a Hubble constant of $70 \text{ km s}^{-1} \text{ Mpc}^{-1}$ or $h_{70} = 1$ as well as cosmological parameters of $\Omega_{m0} = 0.28$ and $\Omega_{\Lambda 0} = 0.72$, we imply an angular diameter distance of $519 h_{70}^{-1} \text{ Mpc}$, a luminosity distance of $678 h_{70}^{-1} \text{ Mpc}$ and a scale of $151.2 h_{70}^{-1} \text{ kpc}$ per arcmin.

Although we will measure this cluster’s properties at the virial radius, we must make rather coarse spatial bins to do so. Thus we can not measure the actual virial radius with much precision. As a point of reference we adopt an often used nominal value, r_{200} , which is the radius within which the cluster average density is 200 times the critical density needed to halt the expansion of the universe. For our cosmology

$$r_{200} = 2.59 h_{70}^{-1} \sqrt{\langle kT \rangle / 10 \text{ keV}} \text{ Mpc}, \quad (1)$$

in which $\langle kT \rangle$ is the cluster average temperature (Henry et al. 2009). An overdensity of 200 is contained within the virialized region of a spherical collapse in an Einstein-de Sitter universe at all red-shifts. Generalizing to a spherical collapse for our adopted cosmology at the red-shift of A1413, gives an overdensity of 109 for the virialized region (Henry 2000). However r_{109} is only 22% larger than r_{200} . So for comparison with previous work we adopt the latter as the nominal virial radius.

The average temperature of A1413 integrated over the radial range of 70 kpc to r_{500} is

7.38 ± 0.11 keV (Vikhlinin et al. 2006), where r_{500} is defined analogously to r_{200} , implying $r_{200} = 2.24 h_{70}^{-1}$ Mpc or 14'.8. Previous observations indicate the cluster is relaxed and there are high quality temperature and mass radial profiles available from both XMM-Newton and Chandra (Pointecouteau et al. 2005; Vikhlinin et al. 2006). There is some disagreement about the mass profile of A1413 in these two works. Pointecouteau et al. (2005) find $r_{500} = (1.13 \pm 0.03) h_{70}^{-1}$ Mpc and $M_{500} = (4.82 \pm 0.42) \times 10^{14} h_{70}^{-1} M_{\odot}$, while Vikhlinin et al. (2006) find $(1.34 \pm 0.04) h_{70}^{-1}$ Mpc and $(7.79 \pm 0.78) \times 10^{14} h_{70}^{-1} M_{\odot}$, respectively, where M_{500} is the mass within r_{500} . Note that both observations measure the temperature out to r_{500} so the disagreement is not due to uncertainties in extrapolation.

Throughout this paper, errors are at 90% confidence for one interesting parameter otherwise noted.

2. Observations

2.1. Suzaku

We observed the northern region of A1413 with the Suzaku XIS detectors. In table 1, we give the details of our observation, and in figure 1(a), we show the XIS field of view (FOV) superimposed on the XMM-Newton image of A1413. The XIS instrument consists of 4 CCD chips; one back-illuminated (BI: XIS1) and three front-illuminated (FI: XIS0, XIS2, XIS3), with each is combined with an X-ray telescope (XRT). The IR/UV blocking filters had accumulated a significant contamination by the time of the observation since its launch (July 2005); we include its effects on the effective area in our analysis. The XIS was operated with normal clocking mode, in 5×5 or 3×3 editing modes. The spaced-row charge injection (SCI) was not applied, and all the four CCDs were working at the time of the observation.

We show the FI+BI image in the 0.5–5 keV energy band in figure 1(b). The non X-ray background (NXB), cosmic X-ray background (CXB), and the Galactic background components (GAL) are subtracted as described below, and the result smoothed by a 2-dimensional gaussian with $\sigma = 16''$ are shown. The image is corrected for exposure time variations, but not for vignetting. Screening requirements are $\text{COR2} > 8$ GV and $100 < \text{PINUD} < 300$ cts s^{-1} , where COR2 is the cut-off-rigidity calculated with the most recent geomagnetic coordinates and PINUD is the count rate from the upper level discriminatory of the Hard X-ray Detector (HXD) PIN silicon diode detectors (see Tawa et al. 2008). The circles with 70'' and 125'' radii enclose excluded point sources. The small white circles indicate point sources detected in the XMM-Newton data. Blue circles show sources selected by eye in the Suzaku image.

We used HEASoft ver 6.4.1 and CALDB 2008-06-21 for all the Suzaku analysis presented here. We extracted pulse-height spectra in five annular regions from the XIS event files. The inner and outer radii of the regions were 2'.7 – 7', 7' – 10', 10' – 15', 15' – 20', and 20' – 26', respectively, measured from the XMM-Newton surface brightness peak of A1413 at (R.A., Dec.)

Table 1. Log of Suzaku observations of Abell 1413

Observation ID	800001010
Date of observation	2005-Nov-15 19:54:46 – 2005-Nov-18 14:14:45
Exposure time (ks)	
(COR2 > 0 GV)	XIS0:107.4, XIS1:108.0, XIS2:107.5, XIS3:107.6
(COR2 > 8 GV)	XIS0: 76.1, XIS1: 76.4, XIS2: 76.2, XIS3: 76.2
(COR2 > 8 GV and 100 < PINUD < 300 cts s ⁻¹)	XIS0: 71.9, XIS1: 72.0, XIS2: 72.0, XIS3: 72.0
(R.A., Dec.) in J2000 *	(11 ^h 55 ^m 19 ^s .0, 23°24′30″)
XIS mode	5 × 5 / 3 × 3, normal clocking, window off, SCI off
N _H	2.19 × 10 ²⁰ cm ⁻² (Dickey & Lockman 1990)

* Average pointing direction of the XIS, shown by the RA_NOM and DEC_NOM keywords of the FITS event files.

= (11^h55^m18^s.7, 23°01′48″) in J2000. We analyzed the spectra in the 0.5–10 keV range for the FI detectors and 0.4–10 keV for the BI detector. In the the 2′.7 – 7′ annulus, we ignored the energy band 5–7 keV for the FI detectors when we analyzed the spectra, because those data were affected by Mn-K_α (5.9 keV) X-rays from the ⁵⁵Fe calibration source. In other annuli, positions of the calibration sources themselves were masked out using the *calmask* calibration database (CALDB) file.

2.2. XMM-Newton

We analyzed an image in the energy band 0.35–1.25 keV taken with XMM-Newton (Pratt & Arnaud 2002). This observation was carried out in June 2000 (OBSID: 0112230501). The exposure time was 25.7 ks (MOS1,MOS2). SAS ver 6.0 and HEASoft ver 6.4.1 were used for the analysis. XMM-Newton has much higher spatial resolution compared to Suzaku. We used this image as input for the response simulators and to find point sources. Pratt & Arnaud (2002) derived a ratio of minor to major axis to be 0.71 and a position angle 2°26′ based on the XMM data. Since Suzaku coverage is limited in the north section of the cluster as shown in figure 1, we did not include the cluster ellipticity in our analysis.

3. Background Analysis

Accurate estimation of the background is particularly important when constraining the ICM surface brightness and temperature in the outer region of clusters. We assumed that the background is comprised of three components: non-X-ray background (NXB), cosmic X-ray background (CXB) and Galactic emission (GAL), which itself is comprised of two components. In this section we describe how we estimate all these background components.

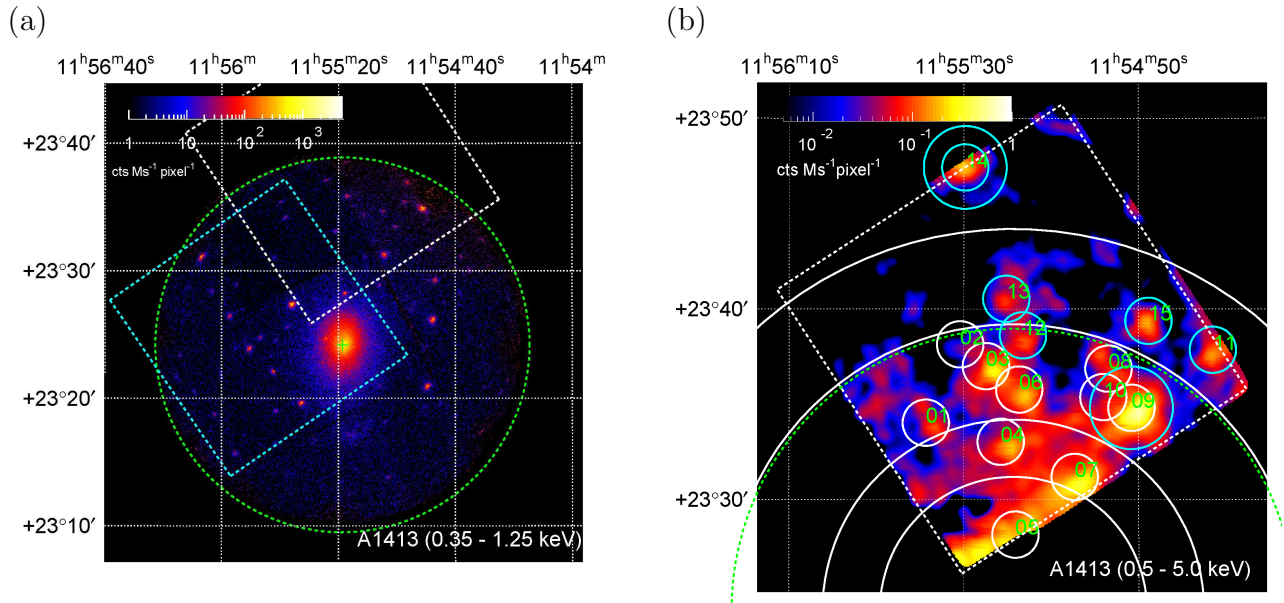


Fig. 1. (a) XMM-Newton MOS1 + MOS2 image of A1413 in the 0.35–1.25 keV band. The image is corrected for exposure, vignetting and background. The white and blue boxes show the fields of view of the Suzaku XIS and Chandra ACIS (Vikhlinin et al. 2006). The green circle shows r_{200} of $14'.8$. Color scale unit is $\text{cts Ms}^{-1} \text{ pixel}^{-1}$ (1 pixel = $2''.49 \times 2''.49$). (b) Background subtracted Suzaku FI+BI image of the outskirts of A1413 in the 0.5–5 keV band smoothed by a 2-dimensional gaussian with $\sigma = 16''$. The image is corrected for exposure time but not for vignetting. Color scale unit is $\text{cts Ms}^{-1} \text{ pixel}^{-2}$ (1 pixel = $1''.04 \times 1''.04$). COR2 > 8 GV and $100 < \text{PINUD} < 300 \text{ cts s}^{-1}$ screening was applied. The ^{55}Fe calibration source regions are also included in the figure, because they have negligible counts in this energy band. Large white circles denote $7'$, $10'$, $15'$, and $20'$ from the surface brightness peak of the XMM-Newton image. Small white and blue circles show the excluded point sources.

3.1. Point Source Analysis

We want to excise point sources because we are only interested in this paper in the ICM. However, since the CXB is comprised of faint point sources, we then need to correct the background level for the resolved sources. This and the next section describe the procedure we used for these tasks.

We used the XMM-Newton image to detect point sources in the XIS FOV because its spatial resolution ($14''$ half power diameter; HPD) is better than Suzaku’s ($2'$ HPD). We detected 10 point sources using *wavdetect* of CIAO, and extracted source and background spectra by setting the extraction radius of $33''$ and $33'' - 66''$, respectively. First, we checked that the MOS1 and MOS2 spectra of each source were consistent. Then we summed the MOS1 and MOS2 spectra to increase the statistics, and fitted the spectrum of each source to evaluate individual spectral parameters. Finally we added the spectra of all the point sources to estimate how much of the CXB these sources resolve. We fitted the spectra by *wabs* \times *pegpwrlw*. The best-fit parameters for the individual point sources and their sum are shown in table 2. We obtained $\chi^2/\text{dof} = 87.2/77$ for the power-law fit to the combined spectrum

(figure 2(a)), indicating a reasonable spectral fit. The photon index is $\Gamma = 1.92 \pm 0.09$ and the flux is $3.23_{-0.44}^{+0.48} \times 10^{-13}$ erg cm⁻² s⁻¹.

We also searched for point sources located outside of the XMM-Newton field with Suzaku, finding an additional 5 sources by eye. These sources all show statistical significance higher than 3.9σ against the brightness fluctuation around individual sources. We performed spectral fits to all the point sources with Suzaku according to the following procedure. The source photons came from a circle of 40'' radius with encircling annular background region of 40'' – 100'' radii. We selected the source regions so they did not overlap each other. These source and background areas could be slightly different among the detectors and sources due to filtering by the *calmask* regions and the presence of hot pixels. We added the FI spectra from XIS0, XIS2, and XIS3 detectors, and summed the BACKSCAL keyword in the FITS header, which correspond to the area of extraction region, A_{sr} or A_{bg} . Then, we carried out spectral fits for the FI and BI spectra simultaneously using the same spectral model as before, first for the individual sources and then the sum of all the point sources.

We show the best-fit parameters for the individual point sources and their sum in table 2 except for sources 04, 05, and 08, because they were faint so that we could not estimate their background reasonably. Obtained fluxes of the sources are slightly affected by leaked photons of the target to the surrounding background regions. To correct for this effect, we calculated the ratio, f_{leak} , of the leaked photons in each background region to the detected photons in the source region using the “*xissim*” FTOOL (Ishisaki et al. 2007). We corrected the original source flux by multiplying a factor $1/(1 - f_{\text{leak}} A_{\text{sr}}/A_{\text{bg}}) \simeq 1/(1 - 0.2 f_{\text{leak}})$ in the F_X columns of Suzaku in table 2. Figures 2(b) and (c) show the combined spectra of all sources for FI and BI. We obtained $\chi^2/\text{dof} = 113.1/117$ for the power-law fit to the combined spectrum, indicating a reasonable spectral fit, too. The photon index is $\Gamma = 1.82 \pm 0.12$ and the flux is $4.83_{-0.56}^{+0.60} \times 10^{-13}$ erg cm⁻² s⁻¹ (2–10 keV).

The number of sources we found and their total flux are consistent with that expected from the $\log N$ – $\log S$ relation summarized in figure 20 of Kushino et al. (2002). The detected sources ranges from $\sim 10^{-14}$ to $\sim 10^{-13}$ erg cm⁻² s⁻¹. We excised all the point sources detected in either the Suzaku or XMM-Newton observations. Normally we excluded a region of 70'' radius but used 125'' radius for two sources (09 and 14 in table 2).

3.2. Cosmic X-ray Background

An ICM temperature measurement in the outer regions of a cluster is very sensitive to the CXB level. We took the 100% CXB surface brightness to be $I_0 = 6.38 \times 10^{-8}$ erg cm⁻² s⁻¹ sr⁻¹ based on the ASCA-GIS measurements (Kushino et al. 2002). Moretti et al. (2008) summarized measurements (Gruber et al. 1999; McCammon et al. 1983; Gendreau et al. 1995; Vecchi et al. 1999; Kushino et al. 2002; Revnivtsev et al. 2003; DeLuca et al. 2004; Revnivtsev et al. 2005; Hickox et al. 2006) of the CXB level, including their new result with *XMM-Newton*. The

Table 2. Best-fit parameters of detected point sources.

Source		FI+BI (Suzaku)*				MOS1+MOS2 (XMM-Newton)†		
ID	(R.A., Dec.) in J2000	Γ	F_x^\ddagger	χ^2/dof	f_{leak}	Γ	F_x^\ddagger	χ^2/dof
01	(11 ^h 55 ^m 38 ^s 7, 23°34′02″)	2.5 ^{+1.3} _{-0.8}	< 2.4	28.0/18	1.53	1.9 ^{+0.5} _{-0.4}	2.4 ^{+1.8} _{-1.2}	16.6/17
02	(11 ^h 55 ^m 30 ^s 8, 23°38′09″)	1.7 (fixed)	< 2.1	14.7/12	1.41	1.9 ^{+0.6} _{-0.5}	2.3 ^{+2.3} _{-1.4}	5.7/12
03	(11 ^h 55 ^m 24 ^s 9, 23°37′00″)	2.2 ^{+0.5} _{-0.4}	1.6 ^{+0.8} _{-0.6}	37.4/30	1.34	1.7 ^{+0.6} _{-0.5}	1.6 ^{+1.6} _{-1.0}	11.2/9
04	(11 ^h 55 ^m 21 ^s 6, 23°33′02″)					1.8 ^{+0.3} _{-0.3}	3.6 ^{+1.6} _{-1.3}	11.1/24
05	(11 ^h 55 ^m 18 ^s 2, 23°28′10″)					1.1 ^{+0.4} _{-0.4}	5.9 ^{+2.9} _{-2.4}	63.6/58
06	(11 ^h 55 ^m 17 ^s 3, 23°35′47″)	1.4 ^{+0.4} _{-0.4}	4.2 ^{+1.6} _{-1.4}	28.1/27	1.39	2.0 ^{+0.2} _{-0.2}	5.0 ^{+1.7} _{-1.4}	28.2/28
07	(11 ^h 55 ^m 04 ^s 6, 23°31′11″)	1.9 ^{+0.3} _{-0.3}	4.7 ^{+2.1} _{-1.9}	39.2/37	1.26	2.1 ^{+0.2} _{-0.2}	4.1 ^{+1.2} _{-1.0}	40.9/37
08	(11 ^h 54 ^m 56 ^s 9, 23°36′52″)					1.3 ^{+0.5} _{-0.5}	6.8 ^{+4.4} _{-3.1}	5.4/5
09	(11 ^h 54 ^m 51 ^s 7, 23°34′49″)	1.7 ^{+0.2} _{-0.1}	16.0 ^{+2.6} _{-2.4}	79.1/58	1.43	2.2 ^{+0.2} _{-0.2}	8.1 ^{+2.4} _{-2.1}	42.5/41
10	(11 ^h 54 ^m 58 ^s 1, 23°35′23″)	1.7 (fixed)	< 1.8	18.0/17	1.21	1.7 ^{+1.3} _{-1.2}	1.1 ^{+2.9} _{-1.1}	5.1/7
11	(11 ^h 54 ^m 33 ^s 0, 23°37′51″)	1.7 ^{+0.6} _{-0.5}	3.1 ^{+2.3} _{-1.9}	13.5/13	1.24			
12	(11 ^h 55 ^m 16 ^s 5, 23°38′37″)	2.0 ^{+0.7} _{-0.5}	1.06 ^{+0.8} _{-0.6}	15.7/19	1.44			
13	(11 ^h 55 ^m 20 ^s 3, 23°40′32″)	0.1 ^{+1.0} _{-1.0}	< 2.8	18.7/18	1.44			
14	(11 ^h 55 ^m 29 ^s 7, 23°47′26″)	2.0 ^{+0.7} _{-0.5}	2.7 ^{+1.7} _{-1.3}	22.4/14	1.28			
15	(11 ^h 54 ^m 47 ^s 7, 23°39′23″)	1.5 ^{+0.3} _{-0.3}	6.6 ^{+2.0} _{-1.8}	23.2/19	1.43			
Total		1.82 ^{+0.12} _{-0.12}	48.3 ^{+6.0} _{-5.6}	113.1/117	1.36	1.92 ^{+0.09} _{-0.09}	32.3 ^{+4.8} _{-4.4}	87.2/77

* Source–04, 05, and 08 are excluded because they exhibited negative counts after the background subtraction.

† Source–11, 12, 13, 14, and 15 are out of MOS1 and MOS2 FOVs.

‡ Unit of flux is 10^{-14} erg cm⁻² s⁻¹ (2–10 keV).

measured CXB surface brightnesses show a significant range from the HEAO1 value of $(5.41 \pm 0.56) \times 10^{-8}$ erg cm⁻² s⁻¹ sr⁻¹ (Gruber et al. 1999) to $(7.71 \pm 0.33) \times 10^{-8}$ erg cm⁻² s⁻¹ sr⁻¹ with SAX-MECS (Vecchi et al. 1999) in the 2–10 keV band. Recent measurements show the flux to be within about 10% of the level reported by Kushino et al. (2002).

We estimated the remaining CXB surface brightness after the above point-source subtraction by the following three methods: (1) subtracting the summed point source fluxes measured with Suzaku from the 100% CXB, (2) subtracting the summed point source fluxes estimated using the log N –log S relation, and (3) fitting a power-law model to the diffuse emission in the 20′ – 26′ region after the point sources are excised.

In case (1), we subtracted contribution of the excised sources of $1.80_{-0.21}^{+0.22} \times 10^{-8}$ erg cm⁻² s⁻¹ sr⁻¹ from the 100% CXB, dividing $F_X = 4.83_{-0.56}^{+0.60} \times 10^{-13}$ erg cm⁻² s⁻¹ of the Suzaku total by 17′.8 × 17′.8 area of the XIS FOV. In case (2), we calculated the integrated point source flux per steradian from

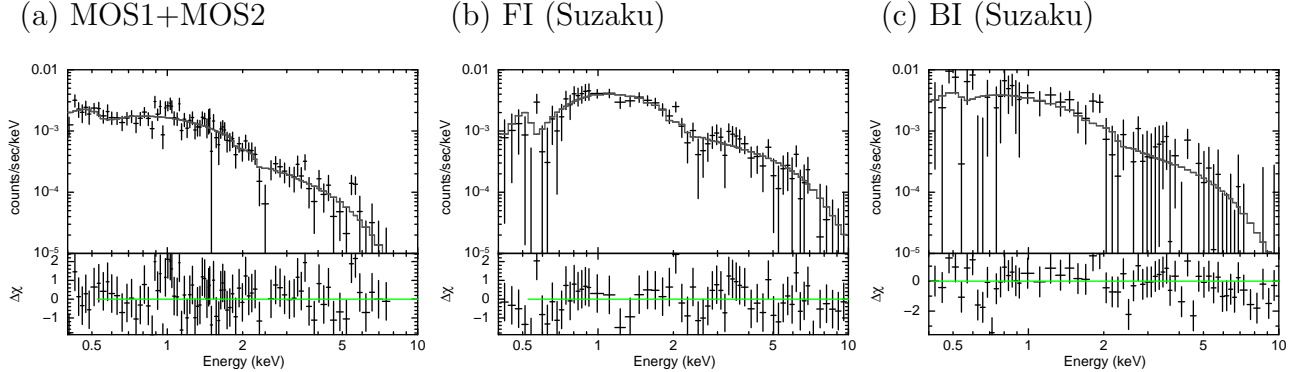


Fig. 2. Power-law model fit to the sum of all point source spectra. (a) MOS1+MOS2, (b) FI, and (c) BI (black: source spectra, grey: best-fit model).

$$I(S > S_0) = \frac{k_0}{\gamma - 2} S_0^{-\gamma+2}, \quad (2)$$

where k and γ are the differential $\log N$ – $\log S$ normalization and slope, respectively. We take nominal values, $k_0 = 1.58 \times 10^{-15} \text{ sr}^{-1} (\text{erg cm}^{-2} \text{ s}^{-1})^{\gamma-1}$ and $\gamma = 2.5$, from Kushino et al. (2002). S_0 is taken as $2 \times 10^{-14} \text{ erg cm}^{-2} \text{ s}^{-1}$, which is slightly higher than our flux limit, because the assumed $\log N$ – $\log S$ in equation (2) does not take into account the flattening of the relation in the fainter flux end. In case (3), we fit the spectra from the solid angle in the $20' - 26'$ annulus that remain after the source excision by a power-law model using a uniform flux ancillary response file (ARF; see section 4.1). The ARF assumes that X-ray photons comes into the detectors uniformly from the sky direction within $20'$ radius from the optical axes of the respective XRTs. The model fit is $apec + wabs \times (apec + powerlaw)$ where the two *apec* components represent the galactic emission. This is the 2T-III model described in section 3.4. In this case, value of the $I_0 - I_X$ column is determined by the spectral fit, and then I_X is calculated assuming $I_0 = 6.38 \times 10^{-8} \text{ erg cm}^{-2} \text{ s}^{-1} \text{ sr}^{-1}$ in table 3.

We summarize our estimations of the remaining CXB surface brightness, $I_0 - I_X$, in table 3. All three methods give consistent results. Hereafter we will use a nominal diffuse cosmic X-ray background spectrum (after subtraction of point sources brighter than $\sim 1 \times 10^{-14} \text{ erg cm}^{-2} \text{ s}^{-1}$ in 2–10 keV band) described by a power-law with a photon index $\Gamma = 1.37$, and surface brightness $4.73 \times 10^{-8} \text{ erg cm}^{-2} \text{ s}^{-1} \text{ sr}^{-1}$ in the 2–10 keV band, which comes from the 2T-III (a) row of the method (3). We adopt this method because it directly measures the quantity of interest in our observations.

To estimate the amplitude of the CXB fluctuations, we scaled the measured fluctuations from Ginga (Hayashida 1989) to our flux limit and FOV area. The fluctuation width is given by the following relation,

$$\frac{\sigma_{\text{Suzaku}}}{I_{\text{CXB}}} = \frac{\sigma_{\text{Ginga}}}{I_{\text{CXB}}} \left(\frac{\Omega_{\text{e,Suzaku}}}{\Omega_{\text{e,Ginga}}} \right)^{-0.5} \left(\frac{S_{\text{c,Suzaku}}}{S_{\text{c,Ginga}}} \right)^{0.25}, \quad (3)$$

where $(\sigma_{\text{Suzaku}}/I_{\text{CXB}})$ means the fractional CXB fluctuation width due to the statistical fluctuation.

Table 3. Estimation of the CXB surface brightness after the point source excision.

	$I_0 - I_X$ *	I_X †	Γ ‡
(1)	$4.58^{+0.22}_{-0.21}$	$1.80^{+0.22}_{-0.21}$	1.41 (fixed)
(2) §	4.15	2.23	1.41 (fixed)
(3) 2T-III (a) 	$4.73^{+0.13}_{-0.22}$	$1.65^{+0.13}_{-0.22}$	$1.37^{+0.04}_{-0.05}$
(3) 2T-III (b) ‡	$4.69^{+0.18}_{-0.18}$	$1.69^{+0.18}_{-0.18}$	$1.40^{+0.05}_{-0.07}$
(3) 2T-III (c) 	$5.16^{+0.12}_{-0.58}$	$1.22^{+0.12}_{-0.58}$	$1.44^{+0.03}_{-0.05}$
(3) contami+20% 	$5.04^{+0.16}_{-0.35}$	$1.34^{+0.16}_{-0.35}$	$1.45^{+0.05}_{-0.05}$
(3) contami-20% 	$4.95^{+0.13}_{-0.33}$	$1.33^{+0.13}_{-0.33}$	$1.44^{+0.06}_{-0.04}$

* Estimated surface brightness of the CXB after the point source excision in unit of 10^{-8} erg cm $^{-2}$ s $^{-1}$ sr $^{-1}$ (2–10 keV).

† Contribution of the resolved point sources in unit of 10^{-8} erg cm $^{-2}$ s $^{-1}$ sr $^{-1}$ (2–10 keV).

‡ Assumed or estimated photon index of the CXB.

§ Surface brightness of 100% of CXB is assumed as $I_0 = 6.38 \times 10^{-8}$ erg cm $^{-2}$ s $^{-1}$ sr $^{-1}$ (2–10 keV). Integrated point source contribution, I_X , is calculated with equation (2). See section 3.2 for details.

|| See section 3.4 for definition. Abundance model is by Anders & Grevesse (1989).

‡ See section 3.4 for definition. Abundance model is by Feldman (1992).

tuation of discrete source number in the FOV. Here, we adopt $\sigma_{\text{Ginga}}/I_{\text{CXB}} = 5\%$, with S_c (Ginga: 6×10^{-12} erg cm $^{-2}$ s $^{-1}$) representing the upper cut-off of the source flux, and Ω_e (Ginga: 1.2 deg 2) representing the effective beam size (or effective solid angle) of the detector. We show the result, σ/I_{CXB} , for each spatial region in table 4.

3.3. Non X-ray Background

The non X-ray background (NXB) spectra were estimated from the Suzaku database of dark earth observations using the procedure of Tawa et al. (2008). We accumulated data for the same detector area, for the same distribution of COR2 as the A1413 observation using the *xisnxbgen* FTOOLS covering 30 days before to 90 days after the observation period of A1413. To increase the A1413 signal-to-noise ratio by reducing the NXB count rate, we required COR2 to be > 8 GV and PINUD to be between 100 and 300 cts s $^{-1}$. After this screening the exposure time dropped from 108 ks to 72 ks, nevertheless the fit residuals were reduced. We also tested other screening criteria, such as COR2 > 8 GV and COR2 > 5 GV, both with no PINUD screening. The former criterion did not affect the final spectral results significantly, but the latter gave different ICM temperatures. To test a possible NXB uncertainty systematic error, we varied its intensity by $\pm 3\%$ as investigated by Tawa et al. (2008).

3.4. Galactic Components

We fit the data in the 20'–26' region to constrain the foreground Galactic emission, using the same uniform-sky ARF as the CXB component. We investigated the best model to use and

Table 4. Properties of the spatial regions used.

Region *	Ω_e † (arcmin ²)	Coverage †	SOURCE_ ‡	σ/I_{CXB} §	FI counts (0.5–10 keV)					
					RATIO_REG	(%)	OBS	NXB	CXB	GAL
2'–7'	...	18.6	14.2%	2.60%	15.4	3,828 ± 62	855 ± 86	560 ± 86	81 ± 9	39.1 ± 3.5%
7'–10'	...	25.6	16.0%	1.49%	13.1	3,568 ± 60	1,241 ± 124	966 ± 127	131 ± 11	65.5 ± 5.3%
10'–15'	...	55.0	14.0%	1.40%	9.0	6,340 ± 80	2,428 ± 242	2,460 ± 220	296 ± 17	81.8 ± 5.3%
15'–20'	...	86.5	15.7%	1.27%	7.1	9,156 ± 96	4,162 ± 416	4,035 ± 288	499 ± 22	95.0 ± 5.6%
20'–26'	...	38.6	4.5%	0.47%	10.7	4,547 ± 67	2,523 ± 252	1,907 ± 204	272 ± 16	103.4 ± 7.3%
Region *	Ω_e † (arcmin ²)	Coverage †	SOURCE_ ‡	σ/I_{CXB} §	BI counts (0.4–10.0 keV)					
					RATIO_REG	(%)	OBS	NXB	CXB	GAL
2'–7'	...	18.4	14.0%	2.60%	15.5	2,042 ± 45	748 ± 75	208 ± 32	85 ± 9	50.9 ± 4.6%
7'–10'	...	25.5	15.9%	1.56%	13.1	2,546 ± 50	1,088 ± 109	392 ± 51	144 ± 12	63.8 ± 5.1%
10'–15'	...	54.9	14.0%	1.41%	9.0	4,447 ± 67	2,277 ± 228	1,012 ± 91	331 ± 18	81.4 ± 5.7%
15'–20'	...	87.4	15.9%	1.32%	7.1	7,425 ± 86	4,418 ± 441	1,857 ± 132	631 ± 25	93.0 ± 6.3%
20'–26'	...	24.6	2.8%	0.37%	13.3	2,984 ± 55	1,954 ± 195	706 ± 94	264 ± 16	98.0 ± 7.5%

* Radii are from the XMM-Newton surface brightness peak in figure 1(a).

† The average value of the four detectors.

‡ $SOURCE_RATIO_REG \equiv Coverage \times \int_{r_{\text{in}}}^{r_{\text{out}}} S(r) r dr / \int_0^{\infty} S(r) r dr$, where $S(r)$ represents the assumed radial profile of A1413.

We confined $S(r)$ to a $60' \times 60'$ region on the sky.

§ $S_c = 1 \times 10^{-14}$ erg cm⁻² s⁻¹ is assumed for all regions.

|| OBS denotes the total observed counts. NXB, CXB and GAL are the estimated counts. $f_{\text{BGD}} \equiv (\text{NXB} + \text{CXB} + \text{GAL})/\text{OBS}$.

the best-fit model parameters. In all cases, we also included a power-law model to represent the CXB. We tried a single temperature thermal plasma model, 1T: $apec + wabs \times powerlaw$, a two temperature model, 2T: $wabs \times (apec_1 + apec_2 + powerlaw)$, and a two temperature model following Tawa et al. (2009), 2T-III: $apec_1 + wabs \times (apec_2 + powerlaw)$. In all models, redshift and abundance of the *apec* components were fixed at 0.0 and 1.0, respectively. The two temperature variants try to model the Local Hot Babble (LHB) and the Milky Way Halo (MWH). We tried three types of the 2T model: both temperatures fixed to 0.204 keV and 0.074 keV given by Lumb et al. (2002), one temperature fixed to 0.074 keV and the second temperature free, both temperatures free. We call the first model as 2T-I, and the second model as 2T-II. The third model did not converge in the fitting, so that we do not discuss it further.

We found that the 1T and 2T-I models gave worse χ^2 values compared with the 2T-II and 2T-III fits. We show the best-fit parameters in table 5 for the 2T-III model, which we adopt. We find that the LHB and MWH temperatures are $0.112_{-0.005}^{+0.009}$ keV and $0.278_{-0.019}^{+0.029}$ keV, respectively. These values are consistent with those obtained by Tawa et al. (2009). We also show in table 5 how the best-fit parameters change as a result of systematic changes in the CXB and NXB levels and of the abundance model used (labeled (a) or (b)). The variations are small: less than $\pm 10\%$ for the temperatures and $\pm 15\%$ for the normalizations. Finally,

Table 5. Galactic components best fit parameters and 90% confidence errors.

	kT_1 (keV)	$Norm_1$ §	S_1	kT_2 (keV)	$Norm_2$ §	S_2
2T-III (a) *	$0.112^{+0.009}_{-0.005}$	$1.994^{+0.147}_{-0.163}$	$0.616^{+0.046}_{-0.050}$	$0.278^{+0.029}_{-0.019}$	$0.194^{+0.051}_{-0.037}$	$0.258^{+0.068}_{-0.050}$
2T-III (b) †	$0.110^{+0.003}_{-0.006}$	$2.199^{+0.148}_{-0.154}$	$0.633^{+0.043}_{-0.044}$	$0.314^{+0.029}_{-0.025}$	$0.222^{+0.045}_{-0.043}$	$0.302^{+0.062}_{-0.059}$
2T-III (c) ‡	$0.113^{+0.003}_{-0.003}$	$1.727^{+0.181}_{-0.101}$	$0.560^{+0.059}_{-0.033}$	$0.260^{+0.964}_{-0.033}$	$0.201^{+0.065}_{-0.028}$	$0.266^{+0.086}_{-0.037}$
NXB+3%, CXB _{MAX} ...	$0.112^{+0.003}_{-0.005}$	$2.015^{+0.180}_{-0.105}$	$0.640^{+0.057}_{-0.033}$	$0.311^{+1.183}_{-0.028}$	$0.197^{+0.042}_{-0.036}$	$0.269^{+0.057}_{-0.049}$
NXB−3%, CXB _{MIN}	$0.111^{+0.014}_{-0.006}$	$2.170^{+0.239}_{-0.203}$	$0.651^{+0.072}_{-0.061}$	$0.319^{+0.706}_{-0.026}$	$0.227^{+0.033}_{-0.074}$	$0.311^{+0.046}_{-0.101}$
contami+20%	$0.111^{+0.002}_{-0.010}$	$2.254^{+0.127}_{-0.222}$	$0.660^{+0.037}_{-0.065}$	$0.269^{+0.818}_{-0.013}$	$0.223^{+0.052}_{-0.044}$	$0.295^{+0.069}_{-0.058}$
contami−20%	$0.113^{+0.005}_{-0.006}$	$1.791^{+0.160}_{-0.152}$	$0.569^{+0.051}_{-0.048}$	$0.286^{+0.920}_{-0.070}$	$0.173^{+0.055}_{-0.039}$	$0.232^{+0.073}_{-0.053}$

* Abundance model is by Anders & Grevesse (1989).

† Abundance model is by Feldman (1992).

‡ Including two gaussian models of O_{VII} and O_{VIII}. Abundance model is by Anders & Grevesse (1989).

§ Normalization of the apec component scaled with a factor of $SOURCE_RATIO_REG/\Omega_e$ in table 4,

$Norm = SOURCE_RATIO_REG/\Omega_e \int n_e n_H dV / (4\pi (1+z)^2 D_A^2) \times 10^{-20} \text{ cm}^{-5} \text{ arcmin}^{-2}$, where D_A is the angular diameter distance to the source.

|| Surface brightness in unit of $10^{-6} \text{ photons cm}^{-2} \text{ s}^{-1} \text{ arcmin}^{-2}$ (0.5–10 keV).

our baseline CXB+GAL model is denoted 2T-III (a), $apec_1 + wabs * (apec_2 + powerlaw)$ with abundances from Anders & Grevesse (1989). We link all parameters of this model, except an overall normalization, when performing the fits for the different spatial regions described in section 4.

3.5. Background Fraction in Each Region

Table 4 presents many properties of the spatial regions we analyzed. The columns are the annular boundaries; the actual solid angle of each region observed, Ω_e ; the coverage fraction of each annulus which is the ratio of Ω_e to the total solid angle of the annulus, *Coverage*; the fraction of the simulated cluster photons which fall in the region compared with the total photons from the entire simulated cluster, $SOURCE_RATIO_REG$; the CXB fluctuations due to unresolved point sources, σ/I_{CXB} ; the observed counts, OBS; the estimated counts for each background component, NXB, CXB, and GAL; and the fraction of background photons given by $f_{BGD} \equiv (NXB+CXB+GAL)/OBS$.

The NXB count rates are calculated from the dark earth data. We simulated the CXB and GAL components spectra using *xissim* with the flux and spectral parameters given in row 2T-III (a) of tables 3 and 5, assuming a uniform surface brightness that fills the field. We plot the NXB and CXB spectra in figures 3 and 4. These spectra gave the count rates in table 4. In the outermost region of 20' – 26', f_{BGD} is consistent with 100%. This confirms the accuracy of our background estimation.

4. Spectral Analysis

4.1. Spatial and spectral responses

We need to prepare the spatial and spectral responses which are necessary for reducing and analyzing our observations of A1413. These responses have complicated properties for extended sources. Indeed they depend on the surface brightness distribution of the source and so are unique for each annular region. Monte Carlo simulators are used to generate some of the responses. The X-ray telescope + XIS simulator is called *xissim*, and the ARF generator using the simulator is called *xissimarfgen* (Ishisaki et al. 2007). We used version 2008-04-05 of the simulator.

A surface brightness distribution is necessary for *xissim* and *xissimarfgen*, because the point spread function (PSF) of the XRT produces an efficiency that is correlated among adjacent spatial cells. Since the XIS FOV did not include the brightness peak of A1413, we used the KBB model of Pratt & Arnaud (2002) to generate the ARF. We numerically projected the KBB 3-dimensional model of the gas density to generate the input surface brightness distribution. Since the ARF describes the detection efficiency as a function of energy, no particular spectral shape is required for input. The effect of the XIS IR/UV blocking filter contamination is included in the ARF based on the calibration of November 2006. The normalization of the ARF is such that the measured flux in a spectral fit for a given spatial region is the flux from the entire input surface brightness. The flux just from the spatial region is the fit flux times the *xissimarfgen* output parameter *SOURCE_RATIO_REG* (table 4). The surface brightness from a given spatial region is then the usual flux from the region divided by the solid angle that subtends from the observer.

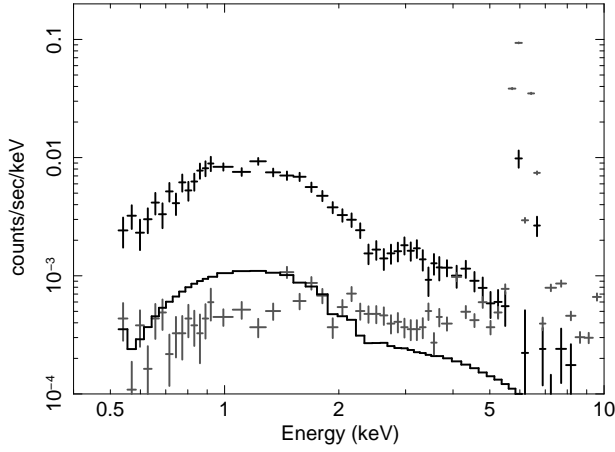
We examined how many photons accumulated in the five annular regions actually came from somewhere else on the sky because of the extended telescope PSF. We show in table 6 the results for the FI+BI detectors in the 0.5–5 keV band. These numbers agree well within 1% for individual sensors and other reasonable energy bands. About 70% of the photons detected in each region actually come from the corresponding sky region. Serlemitsos et al. (2007) gives an upper limit on the error in the simulation at 20'. He reported that the actual stray intensity levels were less than twice those predicted by *xissim* due to the XRT reflector alignment errors and reflections from the pre-collimator blades.

The redistribution matrix file (RMF), which gives the spectral response to a mono-energetic input, is the same for all sources. It was generated with *xisrmfgen* version 2007-05-14. Degradation of the energy resolution is included based on the calibration in November 2006.

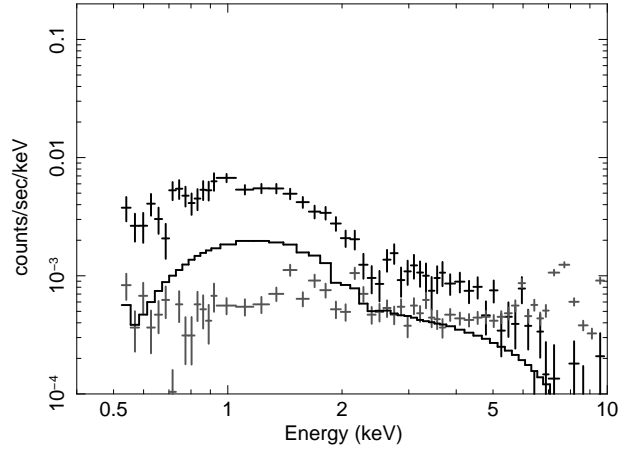
4.2. Model Fitting

We used XSPEC version 12.4.0y for all spectral fitting. The FI and BI spectra were fitted simultaneously. We employed a *wabs* \times *apec* model for the ICM emission of the cluster.

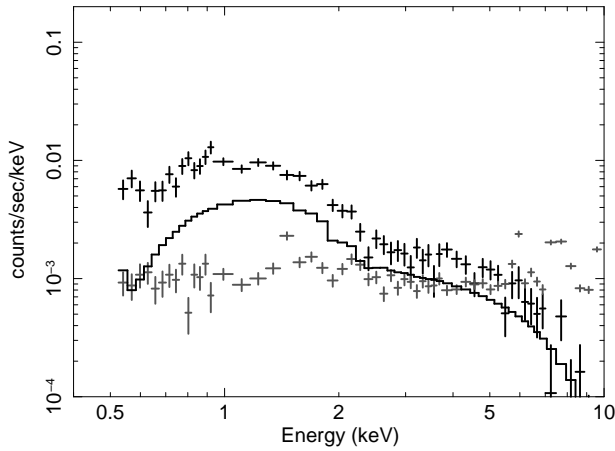
(a) FI, 2'.7 – 7'



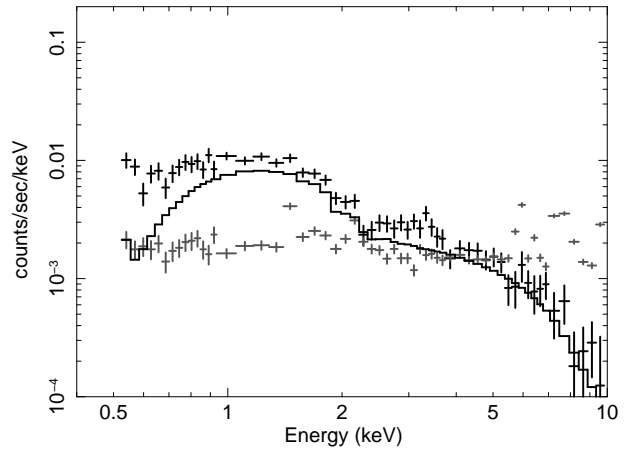
(b) FI, 7' – 10'



(c) FI, 10' – 15'



(d) FI, 15' – 20'



(e) FI, 20' – 26'

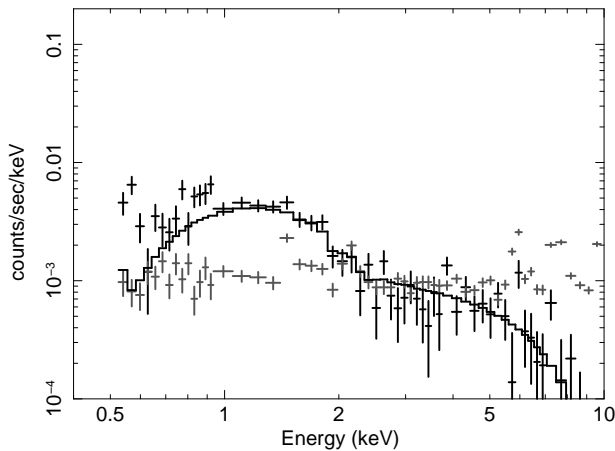
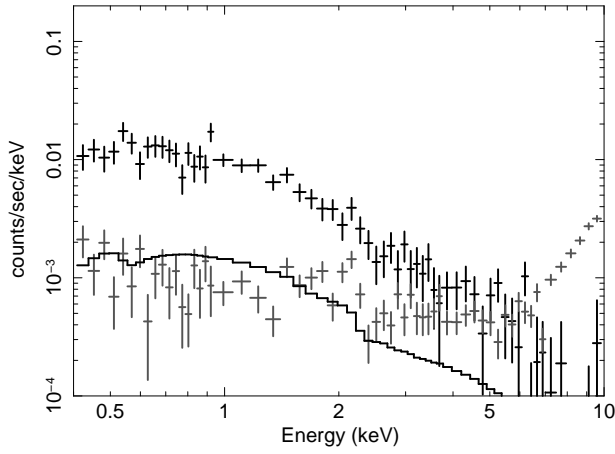
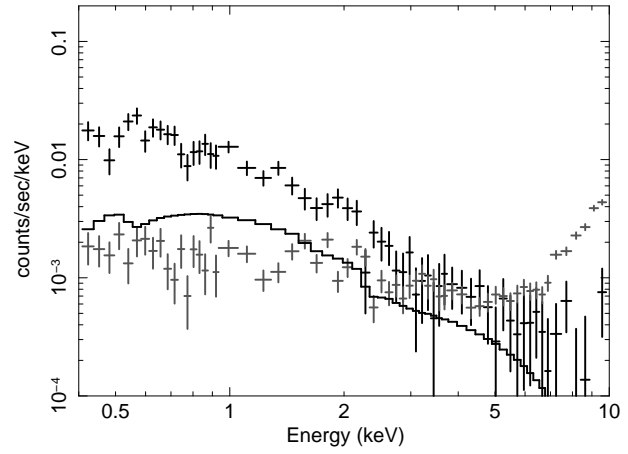


Fig. 3. Spectra for the individual annular regions observed with the FI sensors. The total observed spectrum minus the estimated NXB is the black crosses, the estimated NXB is the grey crosses, and the fitted CXB component is the solid line. The screening used are COR2 > 8 GV and $100 < \text{PINUD} < 300 \text{ cts s}^{-1}$. ^{55}Fe calibration source regions, namely *calmask*, are excluded except for (a).

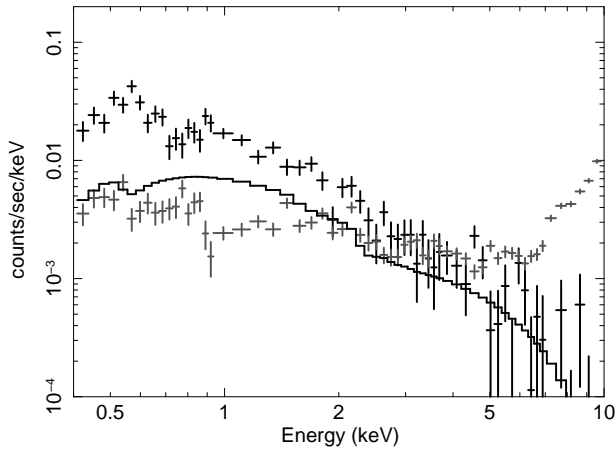
(a) BI, 2'.7 – 7'



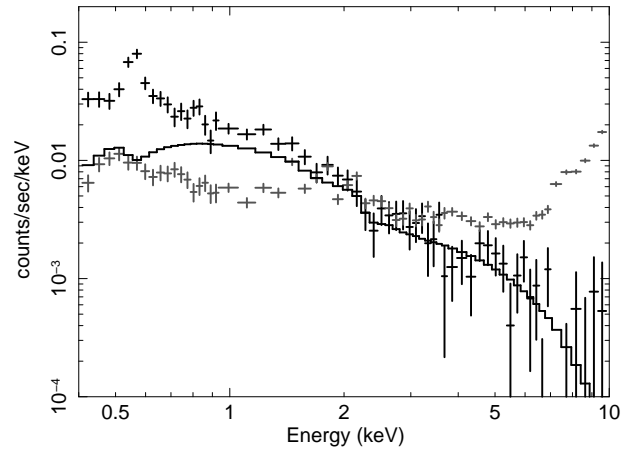
(b) BI, 7' – 10'



(c) BI, 10' – 15'



(d) BI, 15' – 20'



(e) BI, 20' – 26'

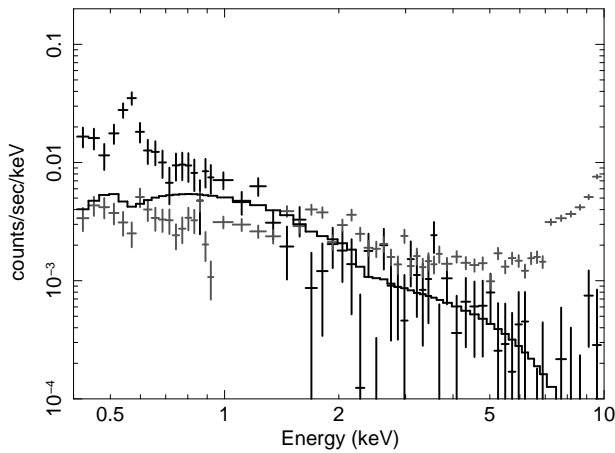


Fig. 4. Same as figure 3, but for the BI detector. All the ^{55}Fe calibration source regions are excluded.

Table 6. Emission weighted radius and estimated fractions of the ICM photons accumulated in detector regions coming from each sky region for FI+BI in the 0.5–5 keV band.

Detector region	Emission weighted radius *	Sky region					
		0–2.7'	2.7–7'	7–10'	10–15'	15–20'	20–26'
2'.7 – 7'	$4.7_{-2.0}^{+2.3}$	21.5%	73.2%	5.1%	0.2%	0.0%	0.0%
7' – 10'	$8.0_{-1.0}^{+2.0}$	16.0%	21.8%	54.9%	7.3%	0.1%	0.0%
10' – 15'	$11.0_{-1.0}^{+4.0}$	6.7%	7.3%	14.0%	67.3%	4.7%	0.0%
15' – 20'	$18.6_{-3.6}^{+1.5}$	4.1%	2.7%	2.7%	16.8%	67.1%	5.4%
20' – 26'	—	6.7%	6.7%	0.0%	0.0%	20.0%	66.7%

* Emission weighted radius from the surface brightness peak of the XMM-Newton.

The *wabs* component models the photoelectric absorption by the Milky Way, parameterized by the hydrogen column density that was fixed at the 21 cm value (Dickey & Lockman 1990). The *apec* is a thermal plasma model. Its fitting parameters are normalization, kT and the ICM abundance. The redshift was fixed at the optical spectroscopic value ($z = 0.1427$). Additional fitting parameters are the two normalizations and temperatures of the GAL components, and the normalization and photon index of the power-law model for the CXB component, as described previously. We did not fit the ICM component in the outermost 20' – 26' region because we can explain the observed spectrum without it, as we show in figure 5(e). This situation was planned as we wanted to have an in-field measurement of the background. In figures 3 and 4, we compare the intensities of the observed spectra minus the NXB to the spectra of the NXB and CXB components. Figure 3(a) shows very strong Mn-K $_{\alpha}$ line at 5.9 keV from the ^{55}Fe calibration source, therefore we ignored the 5–7 keV energy band when we fit the FI spectrum of this annulus.

4.3. Results

In figure 5, we show the best-fit spectra in each spatial region. These figures show the observed spectra after subtraction of the NXB, as well as the best-fit. These figures show that individual spectra are well fitted by the model in each region. The normalization for the ICM component was fixed to zero in the 20' – 26' annulus to estimate the background. The ICM spectra did not show strong emission lines. Because of the low S/N ratio, it was difficult to constrain the model parameters in the 15' – 20' annulus. Therefore, we linked the ICM temperature and abundance in this region to that of the region next interior to it, the 10' – 15' annulus. The best-fit parameters were consistent within the systematic errors for the two regions. The emission weighted average radius for the combined region is $12'.42_{-1'.07}^{+1'.04}$.

Table 7 shows the best-fit parameters for the ICM model in each region. We fitted with two different solar abundances, namely Anders & Grevesse (1989) and Feldman (1992). The

Table 7. Best fitting parameters of the spectral fits with 90% confidence errors for one parameter.

2T-III (a) *	kT (keV)	Abundance (Z_{\odot})	$Norm$ §	S	χ^2/dof
2'.7 – 7'	$7.03^{+1.57}_{-1.11}$	$0.44^{+0.62}_{-0.39}$	$16.35^{+1.16}_{-1.26}$	$5.77^{+0.41}_{-0.45}$	77.4/107
7' – 10'	$4.13^{+0.97}_{-0.65}$	$0.54^{+0.21}_{-0.26}$	$4.53^{+0.30}_{-0.46}$	$2.12^{+0.14}_{-0.22}$	98.7/116
10' – 15'	$3.60^{+0.77}_{-0.62}$	$0.39^{+0.17}_{-0.24}$	$2.29^{+0.19}_{-0.25}$	$0.90^{+0.08}_{-0.10}$	130.1/118
15' – 20'	↑	↑	$0.82^{+0.11}_{-0.26}$	$0.31^{+0.04}_{-0.10}$	109.5/116
20' – 26'	—	—	—	—	152.7/113
Total	—	—	—	—	568.4/570
2T-III (b) †	kT (keV)	Abundance (Z_{\odot})	$Norm$ §	S	χ^2/dof
2'.7 – 7'	$7.14^{+1.62}_{-1.17}$	$0.58^{+0.42}_{-0.40}$	$16.04^{+2.54}_{-0.97}$	$5.75^{+0.91}_{-0.35}$	77.1/107
7' – 10'	$4.41^{+0.95}_{-0.79}$	$0.66^{+0.23}_{-0.36}$	$4.43^{+0.24}_{-0.46}$	$2.11^{+0.11}_{-0.22}$	100.6/116
10' – 15'	$4.03^{+0.91}_{-0.66}$	$0.77^{+0.20}_{-0.51}$	$2.07^{+0.12}_{-0.17}$	$0.90^{+0.05}_{-0.07}$	129.6/118
15' – 20'	↑	↑	$0.72^{+0.09}_{-0.23}$	$0.31^{+0.04}_{-0.10}$	114.7/116
20' – 26'	—	—	—	—	149.2/113
Total	—	—	—	—	571.3/570
2T-III (c) ‡	kT (keV)	Abundance (Z_{\odot})	$Norm$ §	S	χ^2/dof
2.7' – 7'	$7.20^{+1.58}_{-1.20}$	$0.43^{+0.22}_{-0.21}$	$26.54^{+0.92}_{-0.90}$	$9.41^{+0.33}_{-0.32}$	76.7/105
7' – 10'	$4.33^{+0.92}_{-0.70}$	$0.68^{+0.21}_{-0.22}$	$11.02^{+0.66}_{-0.60}$	$5.44^{+0.33}_{-0.30}$	99.8/114
10' – 15'	$3.97^{+0.82}_{-0.66}$	$0.53^{+0.22}_{-0.21}$	$2.07^{+0.14}_{-0.13}$	$0.89^{+0.06}_{-0.06}$	125.2/116
15' – 20'	↑	↑	$0.66^{+0.11}_{-0.13}$	$0.34^{+0.06}_{-0.07}$	104.3/114
20' – 26'	—	—	—	—	154.5/113
Total	—	—	—	—	560.5/562

* Abundance model is Anders & Grevesse (1989).

† Abundance model is Feldman (1992).

‡ Including two gaussian models of O_{VII} and O_{VIII} WHIM emission. Abundance model is Anders & Grevesse (1989)

§ Normalization of the apec component scaled with a factor of $SOURCE_RATIO_REG/\Omega_e$ in table 4,

$Norm = SOURCE_RATIO_REG/\Omega_e \int n_e n_H dV / (4\pi (1+z)^2 D_A^2) \times 10^{-20} \text{ cm}^{-5} \text{ arcmin}^{-2}$, where D_A is the angular diameter distance to the source.

|| Surface brightness in unit of $10^{-6} \text{ photons cm}^{-2} \text{ s}^{-1} \text{ arcmin}^{-2}$ (0.4–10 keV).

Table 8. Same as table 7 except $\text{NXB} \pm 3\%$, CXB_{MAX} and CXB_{MIN} and $\text{contami} \pm 20\%$. Abundance model is Anders & Grevesse (1989).

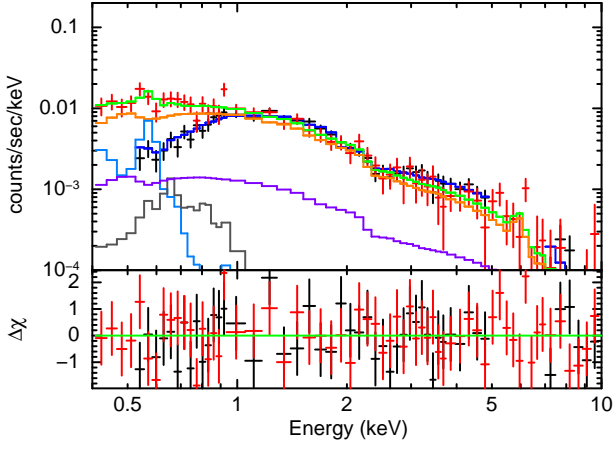
$\text{NXB} - 3\%$, CXB_{MIN}		kT	Abundance	$Norm^*$	S^\dagger	χ^2/dof
		(keV)	(Z_\odot)			
$2'.7 - 7'$	$7.57_{-1.28}^{+1.78}$	$0.47_{-0.31}^{+0.76}$	$16.94_{-1.00}^{+0.70}$	$5.99_{-0.35}^{+0.25}$	78.7/107
$7' - 10'$	$4.84_{-0.81}^{+1.11}$	$0.60_{-0.29}^{+0.32}$	$4.91_{-0.50}^{+0.23}$	$2.34_{-0.24}^{+0.11}$	98.6/116
$10' - 15'$	$4.64_{-0.71}^{+0.88}$	$0.51_{-0.30}^{+0.22}$	$1.07_{-0.18}^{+0.10}$	$0.43_{-0.07}^{+0.04}$	130.6/116
$15' - 20'$	↑	↑	$0.98_{-0.18}^{+0.10}$	$0.41_{-0.08}^{+0.04}$	114.2/116
$20' - 26'$	—	—	—	—	157.1/115
Total	—	—	—	—	579.1/572
$\text{NXB} + 3\%$, CXB_{MAX}		kT	Abundance	$Norm^*$	S^\dagger	χ^2/dof
		(keV)	(Z_\odot)			
$2'.7 - 7'$	$6.60_{-1.08}^{+1.57}$	$0.40_{-0.40}^{+0.86}$	$15.96_{-1.69}^{+0.86}$	$5.51_{-0.59}^{+0.30}$	76.6/107
$7' - 10'$	$3.59_{-0.64}^{+0.80}$	$0.53_{-0.25}^{+0.27}$	$4.16_{-0.72}^{+0.28}$	$1.87_{-0.32}^{+0.13}$	104.3/116
$10' - 15'$	$2.52_{-0.39}^{+0.53}$	$0.35_{-0.19}^{+0.14}$	$2.14_{-0.31}^{+0.18}$	$0.76_{-0.11}^{+0.06}$	130.3/116
$15' - 20'$	↑	↑	$0.53_{-0.19}^{+0.10}$	$0.18_{-0.06}^{+0.04}$	118.6/116
$20' - 26'$	—	—	—	—	150.1/115
Total	—	—	—	—	579.9/572
$\text{contami} + 20\%$		kT	Abundance	$Norm^*$	S^\dagger	χ^2/dof
		(keV)	(Z_\odot)			
$2'.7 - 7'$	$6.89_{-1.05}^{+1.63}$	$0.45_{-0.40}^{+0.60}$	$16.31_{-1.20}^{+1.19}$	$5.74_{-0.42}^{+0.42}$	77.7/107
$7' - 10'$	$4.01_{-0.63}^{+0.93}$	$0.54_{-0.25}^{+0.25}$	$4.54_{-0.45}^{+0.32}$	$2.10_{-0.21}^{+0.15}$	99.0/116
$10' - 15'$	$3.17_{-0.51}^{+0.81}$	$0.29_{-0.17}^{+0.17}$	$2.41_{-0.26}^{+0.22}$	$0.90_{-0.10}^{+0.08}$	131.3/118
$15' - 20'$	↑	↑	$0.84_{-0.24}^{+0.13}$	$0.30_{-0.09}^{+0.05}$	109.6/116
$20' - 26'$	—	—	—	—	153.4/113
Total	—	—	—	—	571.0/570
$\text{contami} - 20\%$		kT	Abundance	$Norm^*$	S^\dagger	χ^2/dof
		(keV)	(Z_\odot)			
$2'.7 - 7'$	$7.08_{-1.13}^{+1.56}$	$0.42_{-0.30}^{+0.59}$	$16.36_{-1.08}^{+0.86}$	$5.78_{-0.38}^{+0.30}$	77.4/107
$7' - 10'$	$4.19_{-0.65}^{+0.97}$	$0.54_{-0.25}^{+0.26}$	$4.49_{-0.45}^{+0.31}$	$2.11_{-0.21}^{+0.15}$	99.0/116
$10' - 15'$	$3.82_{-0.67}^{+0.77}$	$0.44_{-0.26}^{+0.16}$	$2.21_{-0.21}^{+0.17}$	$0.89_{-0.08}^{+0.07}$	128.4/118
$15' - 20'$	↑	↑	$0.79_{-0.23}^{+0.10}$	$0.31_{-0.09}^{+0.04}$	109.1/116
$20' - 26'$	—	—	—	—	153.2/113
Total	—	—	—	—	567.1/570

* Normalization of the apec component scaled with a factor of $\text{SOURCE_RATIO_REG}/\Omega_e$ in table 4,

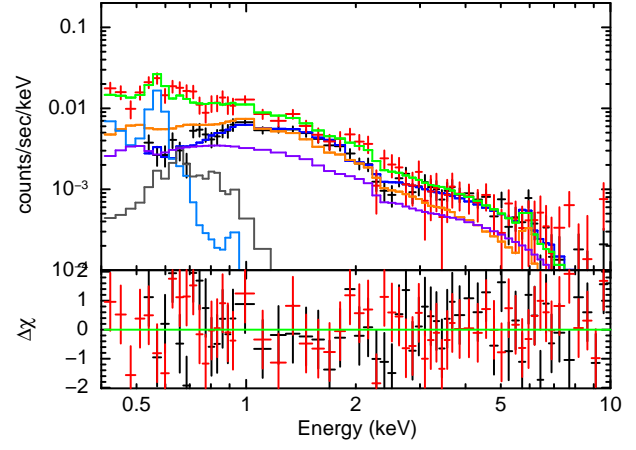
$Norm = \text{SOURCE_RATIO_REG}/\Omega_e \int n_e n_H dV / (4\pi (1+z)^2 D_A^2) \times 10^{-20} \text{ cm}^{-5} \text{ arcmin}^{-2}$, where D_A is the angular diameter distance to the source.

† Surface brightness in unit of $10^{-6} \text{ photons cm}^{-2} \text{ s}^{-1} \text{ arcmin}^{-2}$ (0.4–10 keV).

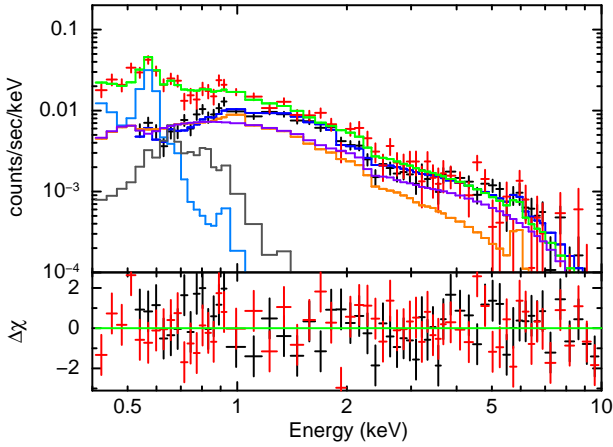
(a) FI+BI, 2'.7 – 7'



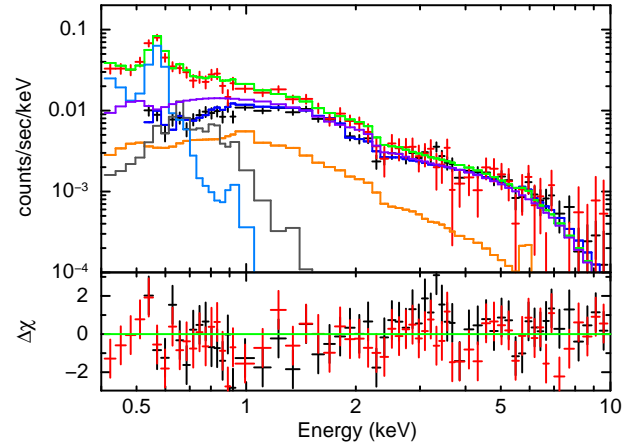
(b) FI+BI, 7' – 10'



(c) FI+BI, 10' – 15'



(d) FI+BI, 15' – 20'



(e) FI+BI, 20' – 26'

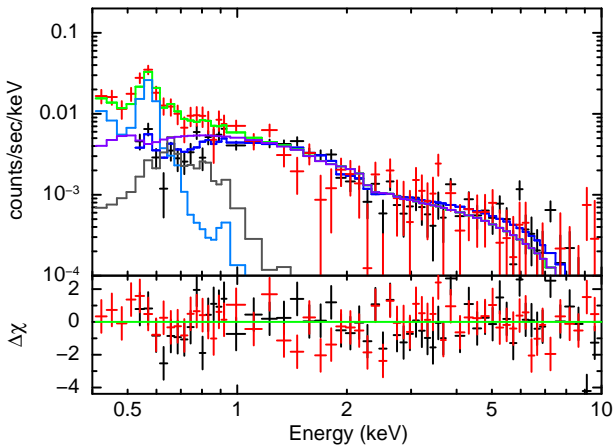


Fig. 5. The upper panels show the observed spectra after subtracting the NXB, that is fitted with the ICM: $wabs \times apec$ model plus the GAL+CXB: $apec_1 + wabs \times (apec_2 + powerlaw)$ model in the energy range 0.5–10 keV for FI and 0.4–10 keV for BI. The annular regions are: (a) 2'.7 – 7', (b) 5' – 10', (c) 10' – 15', (d) 15' – 20', and (e) 20' – 26'. The symbols denote BI data (red crosses), FI data (black crosses), CXB of BI (purple), $apec_1$ of BI (grey), $wabs \times apec_2$ of BI (light blue), ICM of BI (orange), the total model spectra of BI (green), and that of FI (blue). The lower panels show the residuals in units of σ .

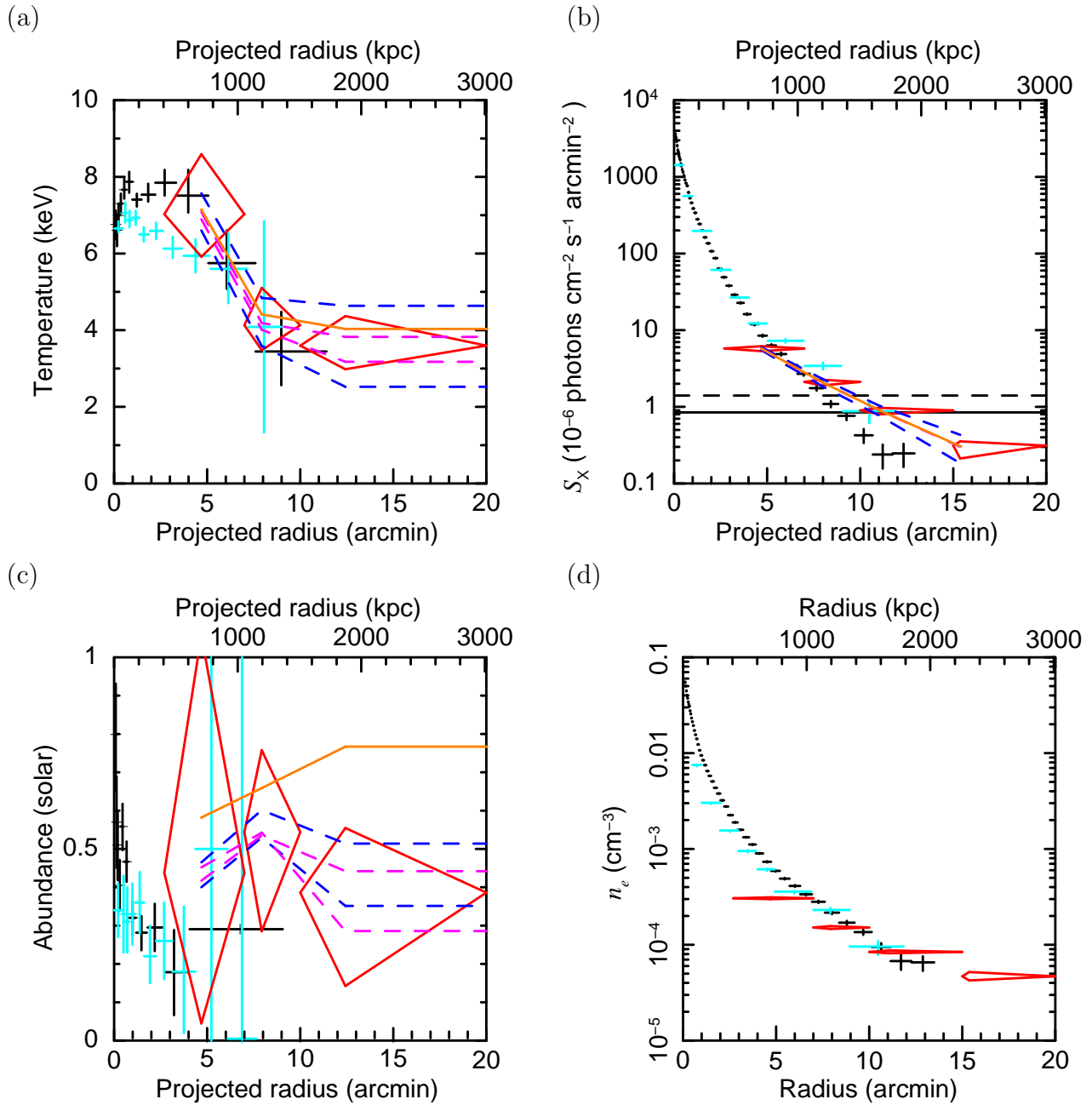


Fig. 6. Radial profiles for (a) temperature, (b) surface brightness (0.4–10 keV), (c) abundance, and (d) 3-dimensional electron density. Red diamonds show our Suzaku results assuming the metal abundances of Anders & Grevesse (1989). Orange line indicates the best-fit profile using the Feldman (1992) abundances. Chandra results by Vikhlinin et al. (2005) are the black crosses, and the cyan crosses are the XMM-Newton results by Snowden et al. (2008). The uncertainty range due to the combined $\pm 3\%$ variation of the NXB level and the maximum/minimum fluctuation of CXB is shown by two blue dashed lines. We show by magenta dashed lines the uncertainties induced by a $\pm 20\%$ uncertainty in the amount of contamination in the IR/UV blocking filters. We also show in panel (b) the CXB level (horizontal dashed line) and the Galactic emission (horizontal solid line).

derived abundance values are higher when we adopt the Feldman (1992) abundance, than the Anders & Grevesse (1989) case, because the Fe abundance relative to H in the former model is lower than the latter.

In figure 6(a), we show temperature profiles observed with Chandra (Vikhlinin et al. 2005), XMM-Newton (Snowden et al. 2008), and Suzaku (this work). These profiles are consistent with each other in the range $7' - 15'$. The Chandra temperatures are about 20% higher than the XMM-Newton values at $2'.7 - 7'$. The tendency that Chandra gives higher temperature than XMM-Newton typically becoming significant above $kT \sim 5-6$ keV is pointed out in figure 12 of Snowden et al. (2008). This discrepancy is due mainly to a Chandra calibration problem, namely the ground calibration of the HRMA effective area had some errors especially at the Ir edge (0.62 keV), and there also was uncertainty about the IR/UV blocking filter contamination. These uncertainties caused a large discrepancy between the Chandra and XMM-Newton measurements for high-temperature clusters. Recent updates of the Chandra CALDB, HRMA AXEFFA version N0008,¹ corrected most of this discrepancy. However, there still remains some differences in cluster temperature by about 10% especially in hot objects. For temperatures below ~ 5 keV, Chandra and XMM-Newton results are mostly consistent with each other.

We therefore used the XMM-Newton temperatures measured by Snowden et al. (2008). In fact, their values are higher than those of Pratt & Arnaud (2002) who used the same data set. This difference may partly be due to the different backgrounds used. Therefore, we assigned rather large errors of 10% even in the inner region of $r < 2'.7$ for these data. We will quantify the systematic error of the Suzaku ICM temperature in the following section.

We plot the related quantities, surface brightness, S_X , and 3-dimensional electron density, n_e , in figures 6(b) and (d). We derived the Chandra surface brightness from the emission measures provided by A. Vikhlinin (private communication). The XMM-Newton surface brightness is from Snowden et al. (2008). The Suzaku surface brightness comes from the normalization of the *apec* model fit. The surface brightness results are consistent with each other within $10'$. In the outer region, the Suzaku surface brightness is significantly higher than the Chandra values. The cause of this discrepancy could be the different region of the cluster observed. In particular, Suzaku observed mainly along the major axis, while Chandra observed the minor axis, as we show in figure 1(a). We obtained the electron density by deprojecting the emission measure with method describe in Kriss et al. (1983).

We show the abundance profile in figure 6(c). Our nominal values are higher than the results of Chandra and XMM-Newton. However, our errors are large and it is difficult to draw firm conclusions.

¹ http://cxc.harvard.edu/ciao4.1/why/caldb4.1.1_hrma.html

4.4. Systematic Errors

To estimate the systematic errors on our electron density, temperature and abundance profiles, we examined the effects of varying the background spectra from their nominal levels. We adopted a systematic error for the NXB intensity of $\pm 3\%$ and the level of the CXB fluctuation was scaled from the Ginga result (Hayashida 1989) as shown in table 4. We considered a $\pm 20\%$ error for the contamination thickness on the IR/UV blocking filters in front of the XIS sensors. As mentioned earlier, we also looked into the effect of the difference between the Anders & Grevesse (1989) and Feldman (1992) abundance models.

We give the outcome of these variations in figure 6 and table 7 for the abundance model comparison, and in figure 6 and table 8 for the other comparisons. Systematic variations of the surface brightness are comparable to its statistical error for all the systematics we examined. The same is true of the temperature except for uncertainties on the UV/IR filter contamination, where the maximum possible range allowed is about 40% larger than the nominal statistical errors. Systematics on the abundance profile were less than the statistical uncertainties except for the outer two spatial bins with the Feldman (1992) abundance models. We conclude from this investigation that our statistical errors also encompass most possible systematic effects.

4.5. Search for WHIM lines

We searched for the warm-hot intergalactic medium (WHIM) which could exist in the filaments of large-scale structures of the universe. The outer regions of clusters may be connected to these filaments and are considered to be promising regions to search for possible WHIM emission.

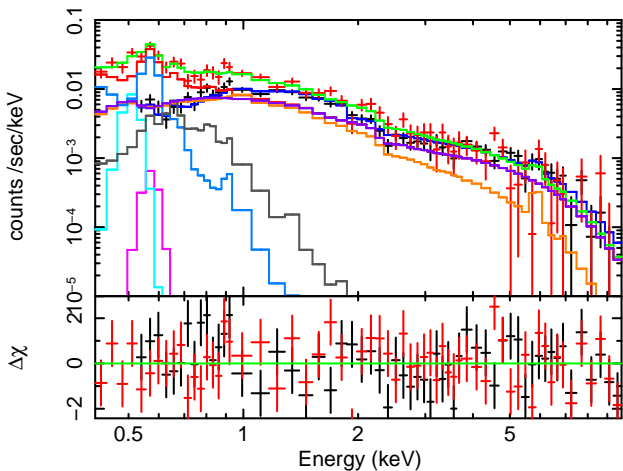
We analyzed the regions $2'.7 - 7'$, $7' - 10'$, $10' - 15'$, and $15' - 20'$. We fitted the FI+BI spectra simultaneously. We added two gaussian lines to model the oxygen emission lines. They had fixed redshifted energies of 0.508 keV (O_{VII}) and 0.569 keV (O_{VIII}), with a fixed width of $\sigma = 0.0$. The ICM spectra fitted with the additional two gaussian lines are shown in figure 7, and table 7(c) gives the fit results. The best temperatures are consistent with the results of the previous fit without the lines. Because redshifted line energies overlapped with those of the Galactic lines, we were unable to distinguish these emission lines directly. Table 9 gives our result for the line intensities which are either 2σ upper limits or marginal detections.

5. Discussion

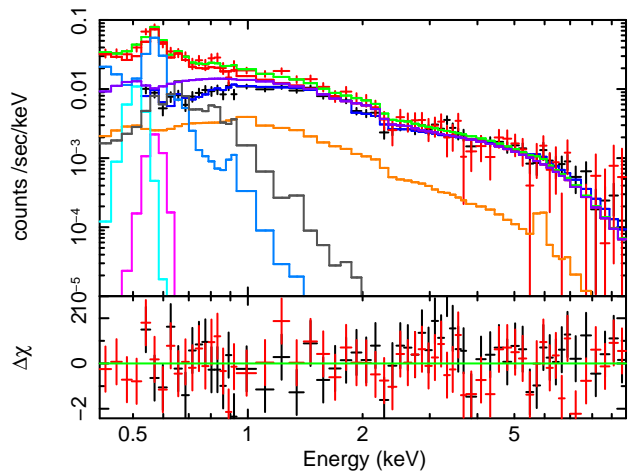
5.1. Temperature and brightness profiles

Numerical simulations indicate that the intracluster gas is almost in hydrostatic equilibrium within the virial radius. For example, Roncarelli et al. (2006) showed that the radial density profiles are smooth out to $\sim 2r_{200}$, while the electron temperature profile has a discontinuity around 1.3–1.5 r_{200} . Eke et al. (1998) performed hydrodynamic simulations in a

(a) FI+BI, 10' – 15'



(b) FI+BI, 15' – 20'

**Fig. 7.** O_{VII} (cyan) and O_{VIII} (pink) line spectra in 10' – 15' and 15' – 20' annuli.**Table 9.** Intensity of redshifted O_{VII} (0.508 keV) and O_{VIII} (0.569 keV) lines in unit of 10^{-6} photons $\text{cm}^{-2} \text{s}^{-1} \text{arcmin}^{-2}$ with 2σ upper limits or 90% confidence errors for a single parameter.

Region	S_{OVIII}	S_{OVII}
2'.7 – 7'	< 0.119	< 0.135
7' – 10'	< 0.075	< 0.091
10' – 15'	< 0.085	$0.094^{+0.059}_{-0.061}$
15' – 20'	< 0.095	$0.081^{+0.048}_{-0.051}$

Λ CDM universe, and discussed the possibility of nonequilibrium around r_{100} because the ratio of kinetic to thermal energy gradually increased from the center to this radius.

Recent X-ray studies of the outer regions of clusters of galaxies with Chandra and XMM-Newton showed significant negative temperature gradients out to a typical radius of r_{500} which is about half of r_{200} (Vikhlinin et al. 2006; Pratt & Arnaud 2002; Snowden et al. 2008). Even though the errors are large, it is significant that our temperatures continue this steady decline, going from about 7.5 keV near the center to ~ 3.5 keV at r_{200} . Recent Suzaku results for the A2204 (Reiprich et al. 2009), PKS0745–191 (George et al. 2008), and A1795 (Bautz et al. 2009) clusters also show a temperature drop to 2–3 keV at r_{200} . The similar temperatures at r_{200} are at least partly due to the fact that all these clusters have similar average temperatures of 5–7 keV. What is likely more significant is the factor of ~ 2 decrease in all cases.

We attempted to compare our measured temperature and surface brightness profiles with theoretical predictions for relaxed clusters. Suto et al. (1998) gave ICM properties for clusters whose potentials follow NFW (Navarro et al. 1996) and modified NFW models, assuming that the ICM can be described by a polytrope. These models have 6 parameters and give a wide range of temperature and density distributions with radius.

We found that, although we could fit either one of the temperature or surface brightness profile with the model, it was not possible to fit both profiles simultaneously despite an exhaustive search of the 6-parameter space. When we fixed the scale radius to be $r_s = 350 \text{ kpc}$ and jointly fit the temperature and brightness profiles, we obtained reduced χ^2 values of 2.0 using only the Chandra data and 3.7 for combined Chandra and Suzaku data, respectively. The likely reason for this result is that the ICM is out of equilibrium in the outer regions of the cluster. We examine this hypothesis in the next section using the entropy profile.

5.2. Entropy profile

Entropy carries information about the thermal history of the ICM, which is thought to be heated by accretion shocks outside the virial radius. The central regions of clusters often exhibit complicated physical phenomena, such as AGN heating and cooling flows, therefore it is difficult to trace the long-term evolution of clusters there. In contrast, the outer regions of clusters is where signatures of the structure formation history can be more clearly seen with the entropy profiles. We use the customary X-ray astronomy definition of entropy as

$$S = kTn_e^{-2/3}. \quad (4)$$

We show the entropy profile derived from our data in figure 8(a). To compare the observed profile with simulation results, we fit the XMM-Newton data from $0'.5$ to $7'$ and the Suzaku data from $7'$ to $20'$ with a power-law model, given by $S \propto r^\gamma$. The XMM-Newton data outside of $7'$ have poorer quality than the Suzaku data, and one Suzaku point inside of $7'$ was also excluded because it is near the field edge with rather low data quality.

We found the best-fit power-law indices to be 0.90 ± 0.10 in $2'$ to $7'$ and 0.97 ± 0.48 in $7'$ to $20'$. The dividing radius of $7'$ corresponds to $0.47 r_{200}$. If we fit all the 7 data points from $2'$ to $20'$, then the slope becomes 0.90 ± 0.12 . These results indicate that there is no difference in the entropy slopes between the inner and outer regions.

Voit (2005) reported $S \propto r^{1.1}$ based on numerical simulations of adiabatic cool gas accretion, and our observational result shows a significantly flatter slope, at least for $r < 7'$. This feature is similar but less pronounced to those reported for A1795 (Bautz et al. 2009) in which the power-law index flattened ($\gamma \approx 0.74$) for $r > 4' \sim 0.15 r_{200}$ and for PKS0745–191 where George et al. (2008) also found a flatter entropy profile in the outer regions. Our result for A1413 suggests that the entropy profile starts to flatten from $\sim 0.2 r_{200}$. To compare the entropy profiles with the simulated slope of 1.1, we divided the entropy by $S \propto r^{1.1}$ as shown in figure 8(b). There appears to be a deviation from the numerical simulation in the range of $r > 0.2 r_{200}$, indicating the flattening of the entropy profiles. We note that the flattening is common to three clusters

We compare our result with a hydrodynamical simulation by Takizawa (1998) that allowed for different electron and ion temperatures. We fit a β -model density profile (parameters n_0, r_c, β) and a polytrope electron temperature profile (parameter polytrope index γ_p) using the

simulated data in his tables 1 and 2. The resulting entropy profile shows a slope of $\gamma_p = 0.42$ in the outer regions for the case of flat universe with $(\Omega_0, \Lambda_0) = (0.2, 0.8)$. Even though this result might be an extreme case, it shows that a difference in the electron and ion temperatures can cause a flattening of the entropy profile.

5.3. Equilibration timescale

Ions carry most of the kinetic energy in the cluster outskirts, and they will be thermalized fairly quickly after accretion shocks or mergers. However, heating the electrons takes a long time because of the inefficient energy transfer between ions and electrons; the equilibration time for electron-ion collisions (t_{ei}) is about 2000 times longer than electron-electron process (t_{ee}) and about 45 times longer than ion-ion relaxation time (t_{ii}).

According to Fox & Loeb (1997), Takizawa (1998), and Rudd & Nagai (2009), the electron-ion timescale including contributions from both protons and He^{2+} is estimated as (Spitzer 1956)

$$t_{ei} \approx 2.0 \times 10^8 \text{ yr} \frac{(T_e/10^8 \text{ K})^{3/2}}{(n_i/10^{-3} \text{ cm}^{-3}) (\ln \Lambda/40)}, \quad (5)$$

where $\ln \Lambda$ is the Coulomb logarithm. We simply assume that ions are initially heated through accretion shocks at r_{200} . In the post-shock region, ions achieve thermal equilibrium with a timescale of t_{ii} after this heating. The ion temperature T_i will then be significantly hotter than the electron temperature T_e . Eventually, thermal energy is transferred from ions to electrons through Coulomb collisions, and T_e will equal T_i after the relaxation time t_{ei} .

We can compare the position-dependent time since the shock heating, t_{elapsed} , with the equilibration timescale t_{ei} . If t_{ei} is longer than t_{elapsed} , then T_e would be expected to be significantly lower than T_i at that position. Denoting the velocity of inward propagation of the shock front as v_{shock} , we obtain

$$r_{200} - r \simeq t_{\text{elapsed}} v_{\text{shock}}. \quad (6)$$

The free-fall velocity of the gas at r_{200} is $v_{\text{ff},200} = \sqrt{2GM_{200}/r_{200}}$. Using the strong shock approximation and neglecting the post-shock gas velocity compared with v_{shock} , Takizawa (1998) found

$$v_{\text{shock}} \simeq \frac{1}{3} v_{\text{ff},200}. \quad (7)$$

Then, we can derive

$$t_{\text{elapsed}} \simeq 3 \frac{r_{200} - r}{v_{\text{ff},200}}, \quad (8)$$

which is independent of M_{200} . In figure 8(c), we show t_{elapsed} and t_{ei} . In the region outside of $r \sim 0.9 r_{200}$, t_{ei} is significantly longer than t_{elapsed} . Based on this calculation, it is likely that T_e and T_i are significantly different in the outskirts of the A1413 cluster.

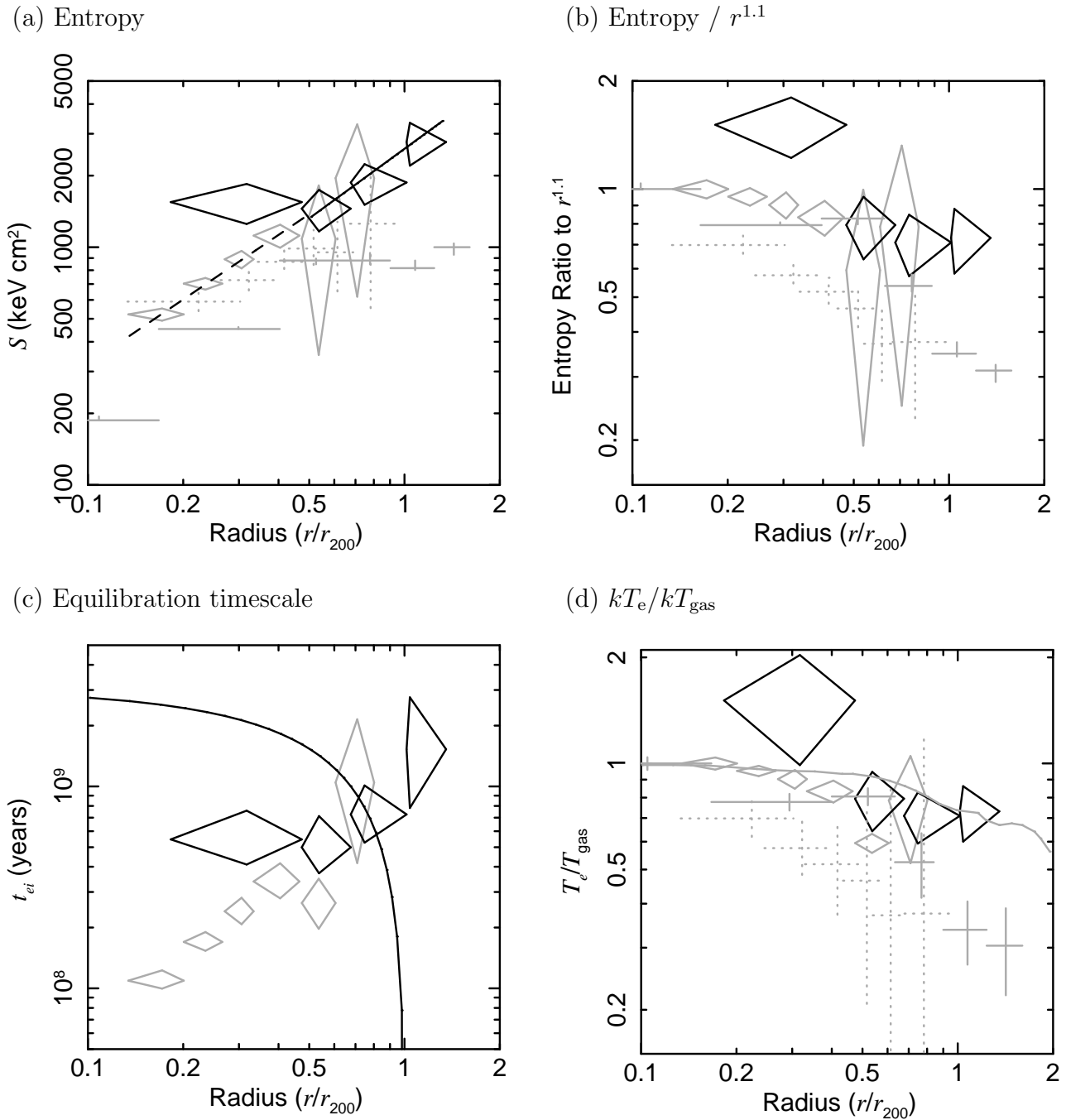


Fig. 8. (a) Entropy profiles (black diamond: Suzaku, grey diamond: XMM-Newton, black solid line: fitted model to Suzaku in $7' - 20'$, black dashed line: fitted model to XMM-Newton in $0'.5 - 7'$, grey solid cross: PKS0745–191, grey dotted cross: A1795). (b) Entropy normalized to $\propto r^{1.1}$ profile. (c) t_{ei} profile (diamonds) compared with t_{elapsed} (black solid line). (d) T_e/T_{gas} profiles compared with the simulated result by Rudd & Nagai (2009).

5.4. Difference between Electron and Ion Temperatures

Fox & Loeb (1997) were the first to investigate the two-temperature nature of the ICM. Takizawa (1998) showed that in a one dimension numerical simulation there existed a significant difference between the electron and ion temperatures, which will affect the entropy profile and the inferred gravitational mass. Recently, Rudd & Nagai (2009) reported the results of simulations which indicated that the temperature difference had a maximum of about 30% at r_{200} . We will examine here a possible deviation between electron and ion temperatures. These studies can help to understand how the cluster gas obtains hydrostatic equilibrium over large volumes.

We define the average gas temperature as,

$$T_{\text{gas}} = \frac{n_e T_e + n_i T_i}{n_e + n_i}, \quad (9)$$

which will change over a typical electron-ion equilibration timescale, t_{ei} . We estimate the average gas temperature, $kT_{\text{gas}} = S n_e^{2/3}$, by assuming a single power-law with $\gamma = 1.1$ for the radial entropy profile, normalized in the cluster inner regions where $T_i = T_e$ because the relaxation times are much shorter there. figure 8(d) shows the ratio of the observed electron temperature to the estimated average gas temperature, where we have adopted $n_i = 0.92 n_e$ (including He^{2+}) for a fully ionized gas with $X = 0.7$ and $Y = 0.28$. Temperature inconsistency between T_e and T_{gas} is possibly larger than the simulation example (Rudd & Nagai 2009).

The rapid T_e decrease in the cluster outer regions may be explained by either the ICM not being in hydrostatic equilibrium or by differences between T_e and T_i . We could determine which interpretation is correct if we could directly estimate T_i from the line width. This measurement should be possible in the near future using the microcalorimeters on the ASTRO-H mission (Takahashi et al. 2008).

5.5. Mass Estimation to r_{200}

We calculated the gravitational mass of A1413 to r_{200} assuming spherical symmetry and hydrostatic equilibrium. From numerical simulations, these assumptions are valid within $\sim 2 r_{200}$ except for the core region at $r < 0.3 r_{200}$, where cooling and heating of AGN give significant effects on the physical state of the gas (Roncarelli et al. 2006; Borgani et al. 2006). Previous X-ray studies mainly showed gravitational mass within r_{500} because of instrumental limitations. In this section, we determine the mass profile in the outer region of A1413.

Assuming hydrostatic equilibrium, the total integrated gravitational mass, $M_{<R}$, within the 3-dimensional radius R is given by (Fabricant et al. 1980)

$$M_{<R} = -\frac{R^2}{\rho_g G} \frac{dP_g}{dR} \quad (10)$$

$$= -\frac{kTR}{\mu m_p G} \left(\frac{d \ln \rho_g}{d \ln R} + \frac{d \ln T}{d \ln R} \right). \quad (11)$$

where G is the gravitational constant, μ is the mean molecular weight of the gas and m_p is the proton mass. We derive the above temperature and gas density profiles using the observed projected temperature and surface brightness profiles. We use the projected temperature directly, but discuss the validity of this assumption below. We calculate the gas density from the normalization of the ICM spectral fit by taking into account the projection effect. The *apec* normalization parameter is defined as $Norm = 10^{-14} \int n_e n_H dV / (4\pi(1+z)^2 D_A^2) \text{ cm}^{-5}$, with D_A the angular diameter distance to the source. We estimated the de-projected $n_e n_H$ values assuming spherical symmetry and a constant temperature in each annular region as described in Appendix 1, and then assumed $n_e = 1.2 n_H$ (excluding He^{2+}) as described above.

Allowing for the possibility of $T_e \neq T_i$, we consider two cases for T : the electron temperature and the average gas temperature. We show the integrated mass profiles in figure 9(a) based on kT_e and kT_{gas} . These profiles are obtained without using any particular model since we perform the needed derivatives by differencing the temperatures and densities of adjacent radial bins. The integrated mass within $13'.2_{-0'.7}^{+4'.3}$, which encompasses r_{200} ($14'.8$) is $(8.8 \pm 2.3) \times 10^{14} M_\odot$ using kT_{gas} . This mass is about 30% larger than that obtained using kT_e of $(6.6 \pm 2.3) \times 10^{14} M_\odot$, although the difference is not statistically significant. The 30% difference in the temperatures propagates almost directly to the same mass difference. Our mass determination agrees with that of Vikhlinin et al. (2006), but not with Pointecouteau et al. (2005). These masses imply an overdensity with respect to critical of 177 ± 47 and 132 ± 47 , where the errors are only from the mass errors.

In the above mass estimation, we assumed that the observed projected temperature is the 3-dimensional value at the observed radius. We need to examine the systematic error caused by this assumption. In the following we denote the true 3-dimensional temperature of the ICM by T_{3d} , which varies with radius. We derive the temperature from the spectral fit is a weighted mean of different temperatures projected along the line of sight. Often the projected temperature is defined as the emission-weighted temperature T_{ew} ,

$$T_{\text{ew}} \equiv \frac{\int n^2 \Lambda(T) T dV}{\int n^2 \Lambda(T) dV} . \quad (12)$$

However, Mazzotta et al. (2004) discussed how the spectral response of an actual instrument implies that T_{ew} can be quite different from what would be measured with that instrument observing a non-isothermal temperature distribution. For a better approximation, they introduced a spectroscopic-like temperature T_{sl} defined as,

$$T_{\text{sl}} \equiv \frac{\int n^2 T^{a-1/2} dV}{\int n^2 T^{a-3/2} dV} , \quad (13)$$

with $a = 0.75$, which empirically gave a good estimate of the T measured with XMM-Newton or Chandra. Rasia et al. (2005) and Shimizu et al. (2006) reported that the difference between T_{ew} and T_{sl} can be as large as 30%. We carried out comparison of observed temperature with kT_{ew} and kT_{sl} in figure 9(a). The difference between kT_{ew} and kT_{sl} takes the largest value of

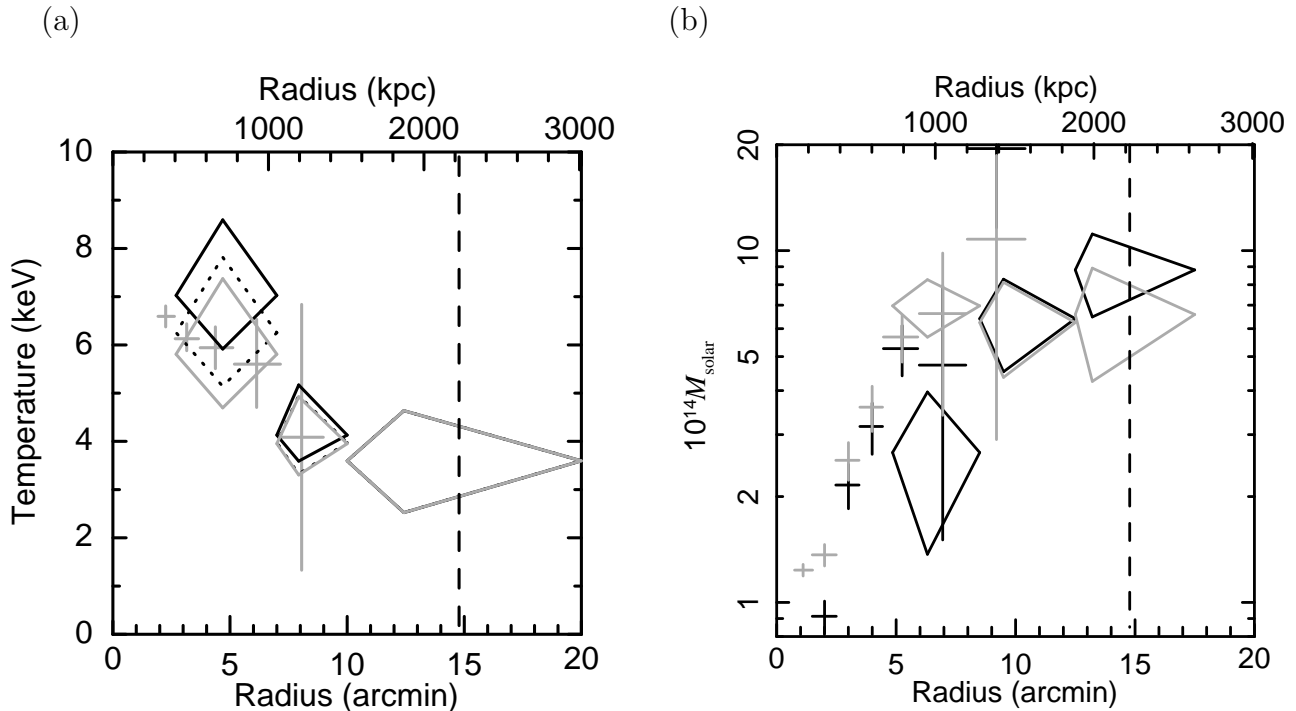


Fig. 9. (a) Comparison of observed temperature (black diamonds) with kT_{ew} (dotted diamonds), and kT_{sl} (grey diamonds). Grey crosses show $kT_{3\text{d}}$ observed with XMM-Newton by Snowden et al. (2008). (b) Integrated mass profile (black diamonds: Suzaku with T_{gas} , grey diamonds: Suzaku with T_e , black crosses: XMM-Newton with T_{gas} , and grey crosses: XMM-Newton with T_e). Vertical dashed line shows $r_{200} = 14'.8$.

about 8.2% in the radius $2'.6 - 7'.0$. These temperatures are consistent with the observed data with XMM-Newton. Taking a conservative value, our mass estimate would be more than 30% different from the true value because of our employment of the observed projected temperature as the 3-dimensional one.

6. Summary

- Northern outskirts of the relaxed cluster of galaxies A1413 was observed with Suzaku in the radial range of $2'.7 - 26'$ covering the virial radius of $r_{200} = 14'.8$. We excised 15 point sources above a flux of $\sim 1 \times 10^{-14}$ erg cm $^{-2}$ s $^{-1}$ (2–10 keV), and the CXB level after the point source excision was evaluated. We quantify all known systematic errors, and show statistical errors are dominant.
- Suzaku detected X-ray emission of the ICM up to the $15' - 20'$ annulus beyond the virial radius. Significant temperature decrease to ~ 3 keV (factor of ~ 2) at r_{200} is confirmed, which was reported in a few other clusters, PKS0745–191 (George et al. 2008), A1795 (Bautz et al. 2009), and A2204 (Reiprich et al. 2009).
- Our entropy profile in the outer region ($> 0.5 r_{200}$) joins smoothly onto that of XMM-

Newton at $0.15\text{--}0.5 r_{200}$, and shows a flatter slope of $\gamma = 0.90 \pm 0.12$ than $\gamma = 1.1$ (Voit 2005) obtained with numerical simulations of adiabatic gas accretion.

- Deviation of the entropy profile from the $r^{-1.1}$ relation would show that electron temperature is not equal to gas temperature in outer region, where equilibration timescale for electron-ion collision, t_{ei} , is longer than the elapsed time after the shock heating, t_{elapsed} .
- The integrated mass of the cluster at the virial radius is approximately $7.5 \times 10^{14} M_{\odot}$ and varies by $\sim 30\%$ depending on temperatures (T_e , T_{gas} , T_{ew} , and T_{sl}) which we use.

We are grateful to S. L. Snowden and A. Vikhlinin for communicating their unpublished results. This work was supported by Grant-in-Aid for JSPS Fellows (20·2427) and the MEXT program ‘‘Support Program for Improving Graduate School Education’’. JPH gratefully acknowledges financial support from NASA grant NNG06GC04G.

References

- Anders, E., & Grevesse, N. 1989, *Geochim. Cosmochim. Acta*, 53, 197
- Bautz, M.W., Miller, E.D., Sanders, J.S., Hayashida, K., Henry, J.P., Hughes, J.P., & Tamura, T., 2009, arXiv:0906.3515v1
- Böhringer, H., et al. 2000, *ApJS*, 129, 435
- Borgani, S., et al. 2004, *MNRAS*, 348, 1078
- Borgani, S., et al. 2006, *MNRAS*, 367, 1641
- Condon, J.J. 1974, *AJ*, 188, 279
- De Grandi, S., & Molendi, S. 2002, *ApJ*, 567, 163
- De Luca, A., & Molendi, S., 2004, *A&A*, 419, 837
- Dickey, J. M., & Lockman, F. J. 1990, *ARA&A*, 28, 215
- Eke, V., R., Navarro, J., F., & Frenk, C., S., 1998, *ApJ*, 503, 569
- Evrard, A. E., Metzler, C. A., & Navarro, J. F., 1996, *ApJ*, 469, 494
- Fabricant, D., Lecar, M., & Gorenstein, P. 1980, *ApJ*, 241, 552
- Feldman, U. 1992, *Phys. Scr.*, 46, 202
- Fox, D., C., & Loeb, A., 1997, *ApJ*, 491, 459
- Gendreau, K.C., Mushotzky, R., Fabian, A.C., et al., 1995, *PASJ*, 47, L5
- George, M.R., Fabian, A. C., Sanders, J. S., Young, A. J., and Russell, H. R., 2008, *MNRAS*, 395, 657
- Gruber, D. E., Matteson, J.L., Peterson, L.E., & Jung, G.V., 1999, *ApJ*, 520, 124
- Hayashida, K. 1989, *PhD. dissertation of Univ. of Tokyo*, ISAS RN 466
- Hayashida, K., Inoue, H., Koyama, K., 1989, *PASJ*, 41, 1373
- Henry, J. P. 2000, *ApJ*, 534, 565
- Henry, J. P., Evrard, A. E., Hoekstra, H., Babul, A., & Mahdavi, A. 2009, *ApJ*, 691, 1307
- Hickox, R.C., & Markevitch, M., 2006, *ApJ*, 645, 95
- Ishisaki, Y., et al. 2007, *PASJ*, 59, 113
- Komatsu, E., & Seljak, U. 2002, *MNRAS*, 336, 1256

Koyama, K., et al. 2007, PASJ, 59, 23
 Kriss, G.A., Cioffi, D.F., & Canizares, C.R., 1983, ApJ, 272, 439
 Kushino, A., Ishisaki, Y., Morita, U., Yamasaki, N. Y., Ishida, M., Ohashi, T., & Ueda, Y. 2002, PASJ, 54, 327
 Loken, C., Norman, M. L., Nelson, E., Burns, J., Bryan, G. L., & Motl, P. 2002, ApJ, 579, 571
 Lumb, D. H., Warwick, R. S., Page, M., & De Luca, A. 2002, A&A, 389, 93
 Markevitch, M., Forman, W. R., Sarazin, C. L., & Vikhlinin, A. 1998, ApJ, 503, 77
 Mazzotta, P., Rasiz, E., Moscardini, L., & Tormen, G., 2004, MNRAS, 354, 10
 McCammon, D., Burrows, D.N., Sanders, W.T., & Kraushaar, W.L., 1983, ApJ, 269, 107
 Mitsuda, K., et al. 2007, PASJ, 59, 1
 Moretti, A., Pagani, C., Cusumano, G. et al., 2008, ArXiv e-prints, 0811.1444M
 Navarro, J. F., Frenk, C. S., & White, S. D. M. 1996, ApJ, 462, 563
 Piffaretti, R., Jetzer, P., Kaastra, J. S., & Tamura, T. 2005, A&A, 433, 101
 Pointecouteau, E., Arnaud, M., & Pratt, G. W. 2005, A&A, 435, 1
 Pratt, G. W., & Arnaud, M. 2002, A&A, 394, 375
 Pratt, G. W., Böhringer, H., Croston, J. H., Arnaud, M., Borgani, S., Finoguenov, A., & Temple, R. F. 2007, A&A, 461, 71
 Rasia, E., Mazzotta, P., Bologani, S., Moscardini, L., Dolag, K., Tormen, G., Diaferio, A., Murante, G., 2005, ApJ, 618, L1
 Reiprich, T. H., et al. 2009, A&A, 501, 899
 Revnivtsev, M., Gilfanov, M., Sunyaev, R., Jahoda, K., & Markwardt, C., 2003, A&A, 411, 329
 Revnivtsev, M., Gilfanov, M., Jahoda, K., & Sunyaev, R., 2005, A&A, 444, 381
 Roncarelli, M., Ettori, S., Dolag, K., Moscardini, L., Borgani, S., & Murante, G. 2006, MNRAS, 373, 1339
 Rudd, D.H., & Nagai, D., 2009, ApJ, 701, L16
 Serlemitsos, P. J., et al. 2007, PASJ, 59, 9
 Shimizu, M., Kitayama, T., Sasaki, S., & Suto, Y. 2006, PASJ, 58, 291
 Snowden, S.L., Mushotzky, R.F., Kuntz, K.D., & Davis, D.S, 2008, A&A, 478, 615
 Spitzer, L.Jr., 1956, Physics of Fully Ionized Gases, New York: Interscience
 Suto, Y., Sasaki, S., Makino, N. 1998, ApJ, 509, 544
 Takahashi, T., et al. 2008, Proc. SPIE, 7011,
 Takizawa, M., 1998, ApJ, 509, 579
 Takizawa, M., & Mineshige, S., 1998, ApJ, 499, 82
 Tawa, N., et al. 2008, PASJ, 60, 11
 Tawa, N., 2008, ISAS Research Note 839
 Vecchi, A., Molendi, S., Guainazzi, M., Fiore, F., & Parmar, A.N., 1999, A&A, 349, L73
 Vikhlinin, A., Markevitch, M., Murray, S. S., Jones, C., Forman, W., & Van Speybroeck, L. 2005, ApJ, 628, 655
 Vikhlinin, A., Kravtsov, A., Forman, W., Jones, C., Markevitch, M., Murray, S. S., & Van Speybroeck, L. 2006, ApJ, 640, 691
 Voit, G.M., 2005, RvMP, 77, 207

Zhang, Y.-Y., Böhringer, H., & Finoguenov, A., 2005, *Adv. Sp. Res.*, 36, 667